J Comput Electron (2009) 8: 225–241
DOI 10.1007/s10825-009-0294-y

A fully coupled scheme for a Boltzmann-Poisson equation solver based on a spherical harmonics expansion

S.-M. Hong · C. Jungemann

Published online: 1 October 2009

Abstract The numerical properties of a deterministic Boltzmann equation solver based on a spherical harmonics expansion of the distribution function are analyzed and improved. A fully coupled discretization scheme of the Boltzmann and Poisson equations is proposed, where stable equations are obtained based on the H-transformation. It is explicitly shown that the resultant Jacobian matrix for the zeroth order component has property M for a first order expansion, which improves the stability even of higher order expansions. The detailed dependence of the free-streaming operator and the scattering operator on the electrostatic potential is exactly considered in the Newton-Raphson scheme. Therefore, convergence enhancement is achieved compared with previous Gummel-type approaches. This scheme is readily applicable to small-signal and noise analysis. As numerical examples, simulation results are shown for a silicon n^+nn^+ structure including a magnetic field, an SOI NMOSFET and a SiGe HBT.

Keywords Boltzmann equation · Spherical harmonics expansion · Small-signal · Noise

1 Introduction

Due to the continuous scaling during several decades, the feature size of semiconductor devices has reached the deca-nanometer range [1]. For such scaled devices, transport cannot be described accurately by momentum based models (drift-diffusion or hydrodynamic models) [2, 3], which fail even in the linear transport regime [4, 5].

In the semiclassical framework the Boltzmann equation gives the most accurate information about device operation [6–9]. The solution of the Boltzmann equation is the distribution function, which is the occupancy of the electron states. Once the distribution function is known, all the measurable quantities can be evaluated. However, it is defined over the six-dimensional phase space (three-dimensional real space and three-dimensional wavevector space). The high dimensionality of the phase space makes solving the Boltzmann equation a very challenging task. Since an analytical solution is not available for the general case, a computational approach is required.

The usual approach for solving the Boltzmann equation is the Monte Carlo approach, where the Boltzmann equation is solved by simulating a stochastic process [10–15]. In this approach, advanced physical models (e.g. full band description [16, 17]) can be easily implemented. However, the Monte Carlo method has many disadvantages due to its stochastic nature [18]. For example, small currents can entail excessive CPU times and it is difficult to perform small-signal analysis in the lower GHz range [19].

A possible alternative is to solve the Boltzmann equation in a deterministic manner without stochastic errors. Its properties are similar to those of the classical TCAD models. Since the distribution function is expanded with specific basis functions, the number of unknown variables after discretization can be very large. As a result, the deterministic approach requires much more computer memory than the Monte Carlo approach. This is the main reason why the application of deterministic Boltzmann equation solvers to devices was hampered for a long time. The rapid advance of

S.-M. Hong · C. Jungemann (✉)
Institute for Microelectronics and Circuits,
Bundeswehr University, 85577 Neubiberg, Germany
e-mail: jungemann@ieee.org

S.-M. Hong
e-mail: hi2ska2@gmail.com

modern computers makes such an approach more and more feasible.

There are many possible ways in the choice of basis functions. For example, the discretization of the entire wavevector space with a three-dimensional grid can be found in [20, 21]. However, the structure of the scattering integral suggests to write the Boltzmann equation in polar coordinates and to use spherical harmonics as basis functions for the angular dependence. Regarding the radial dependence of the distribution function, usually the energy is discretized with a grid. In [22–25], the energy dependence of the distribution function is resolved by an expansion with polynomials.

The idea to expand the distribution with spherical harmonics was among the first methods used to solve the Boltzmann equation by numerical means (e.g. [26]). Since the spherical harmonics expansion was first applied to devices in [27], there have been considerable efforts to improve the physical models. In bulk simulations, some full band effects were included into the lowest-order expansion by Vecchi et al. [28]. Complete inclusion of a full band structure was demonstrated for the valance bands in [29]. Simulations including a magnetic field were reported in [30] for bulk and in [31] for devices. The simulation of a MOSFET with the relevant scattering mechanisms can be found in [32]. Since rare events can be easily calculated in contrast to the Monte Carlo approach, the substrate current for MOSFETs, for example, can be readily calculated [32]. Although restricted to a lowest-order expansion, two-dimensional simulations were already reported in [32, 33]. Two-dimensional simulations with a higher-order expansion appeared only recently in [34]. Impact ionization can be easily implemented. Simulations including some quantum effects were reported in [35].

The order at which the spherical harmonics expansion is truncated has a strong impact on the accuracy of the results. For the bulk case, Hennacy et al. presented higher-order expansions [36, 37]. In the case of one-dimensional devices Rahmat et al. demonstrated a third-order expansion [38]. Later expansions of arbitrary order were reported for such devices in [29]. Box integration for the derivation of the discrete system of equations was introduced and exact current continuity achieved [27, 33, 38]. Without stabilization simulation of realistic semiconductor devices is not possible. The H-transform was developed to stabilize the equations [27]. An upwind discretization have been proposed in [38]. Later a stabilization was introduced [29], which is based on the maximum entropy dissipation scheme [23].

Small-signal analysis is a vital component of modern device simulation. In contrast to the Monte Carlo method, small-signal analysis is possible for devices in the case of the spherical harmonics expansion [35, 39, 40]. Noise can be calculated based either on the Boltzmann equation [41, 42] or Langevin Boltzmann equation [43].

In this paper, we review recent developments and applications of the spherical harmonics expansion method. Compared with previous works for the device simulation by the Maryland group [32, 35–37, 39], the Bologna group [27, 33], and the MIT group [38], the particular focus is on the demonstration of higher-order expansion results for the two-dimensional device, on the stabilization and discretization through a combination of the H-transformation and the maximum entropy dissipation scheme, and on its application to small-signal analysis [31, 34, 44, 45].

The structure of the paper is as follows: In Sect. 2, the underlying theory is described in some detail. The focus is in particular on the stabilization and discretization schemes. In Sect. 3, three examples of applications, magnetotransport in an n^+nn^+ structure, a partially depleted SOI MOSFET, and a SiGe HBT, are considered. Conclusions and future perspectives are given in Sect. 4.

2 Theory

In this work, we consider carrier transport in a two-dimensional SiGe device, possibly under the presence of a constant magnetic field perpendicular to the simulation plane. The position-dependent band edge of the conduction band due to the position-dependent Ge content is taken into account. Electron transport is described by balance equations derived from the Boltzmann equation, while hole transport is described by a simple drift-diffusion model.

2.1 Boltzmann equation and expansion with spherical harmonics

The band structure of the conduction band is of critical importance for electron transport. In this work, we employ the Modena model, in which the conduction band is described by six nonparabolic and elliptical valleys [7, 46]. The parameters of the related scattering mechanisms can be found in [46]. The original momentum space of this model is denoted as $\boldsymbol{k}'$-space.

All calculations are performed in the Herring-Vogt transformed $\boldsymbol{k}$-space [47], since it simplifies the SHE very much [48]. The elliptical valleys are mapped onto spherical ones by the Herring-Vogt transform [7, 47]

$$\boldsymbol{k}^\nu = \hat{T}^\nu \boldsymbol{k}'^\nu, \tag{1}$$

$$\hat{T}^\nu = \begin{pmatrix} T_x^\nu & 0 & 0 \\ 0 & T_y^\nu & 0 \\ 0 & 0 & T_z^\nu \end{pmatrix}, \tag{2}$$

where ν is the index of νth valley, and $\boldsymbol{k}$ and $\boldsymbol{k}'$ are wave vectors in the Herring-Vogt transformed $\boldsymbol{k}$-space and the original $\boldsymbol{k}'$-space, respectively. The nonparabolic band energy ε

relative to the minimum of the conduction band is given by

$$\varepsilon(1+\alpha\varepsilon)=\frac{\hbar^2k^2}{2m_d}, \tag{3}$$

where α is the nonparabolicity factor, m_d the density-of-state mass, and $\hbar$ the Planck constant divided by 2π. The group velocity in the Herring-Vogt transformed space evaluates to

$$\boldsymbol{v}=v(\varepsilon)\boldsymbol{e}_\varepsilon=\frac{1}{1+2\alpha\varepsilon}\frac{\hbar k(\varepsilon)}{m_d}\boldsymbol{e}_\varepsilon, \tag{4}$$

where $\boldsymbol{e}_\varepsilon$ is the unit vector of the spherical coordinate system for the radial direction.

Since we introduce the Herring-Vogt transformation, the partial derivative in the $\boldsymbol{k}'$-space must be transformed. The semiclassical BE, which is modified for the Herring-Vogt transformed $\boldsymbol{k}$-space reads

$$\frac{\partial f}{\partial t}+\frac{1}{\hbar}\hat{T}\boldsymbol{F}\cdot\nabla_{\boldsymbol{k}}f+\hat{T}\boldsymbol{v}\cdot\nabla_{\boldsymbol{r}}f=\check{W}\{f\}, \tag{5}$$

where $f^\nu(\boldsymbol{r},\boldsymbol{k},t)$ is the distribution function for a single spin direction, t the time variable, $\boldsymbol{r}$ the position in real space, and $\check{W}\{f\}$ the single-particle scattering integral. The force is given by

$$\begin{aligned}\boldsymbol{F}^\nu&=\boldsymbol{F}_E^\nu+\boldsymbol{F}_B^\nu\\&=\nabla_{\boldsymbol{r}}\left(-E_c^\nu(\boldsymbol{r})+q\psi(\boldsymbol{r},t)\right)-q\left(\hat{T}^\nu\boldsymbol{v}\right)\times\boldsymbol{B},\end{aligned} \tag{6}$$

where E_c^ν is the position-dependent valley minimum of νth valley of the conduction band measured from the intrinsic level of relaxed silicon, ψ the electrostatic potential, and $\boldsymbol{B}$ the magnetic field. Note that the first term on the right hand side represents the force due to the electric field and a gradient of the band edge, while the second term is due to the magnetic field. The Herring-Vogt transformed force is given by [49]

$$\hat{T}^\nu\boldsymbol{F}^\nu=\hat{T}^\nu\nabla_{\boldsymbol{r}}\left(-E_c^\nu(\boldsymbol{r})+q\psi(\boldsymbol{r},t)\right)-q\boldsymbol{v}\times\grave{\boldsymbol{B}}^\nu, \tag{7}$$

where $\grave{\boldsymbol{B}}^\nu$ is the transformed magnetic field defined as

$$\grave{\boldsymbol{B}}^\nu=\begin{pmatrix}T_y^\nu T_z^\nu & 0 & 0\\ 0 & T_z^\nu T_x^\nu & 0\\ 0 & 0 & T_x^\nu T_y^\nu\end{pmatrix}\boldsymbol{B}. \tag{8}$$

Note that the magnetic force in the Herring-Vogt transformed $\boldsymbol{k}$-space is still perpendicular to the group velocity in that space.

Following the scheme based on the expansion of the distribution function on equienergy surfaces [29], a unique mapping between the $\boldsymbol{k}$-space and the energy space is required. In the case of the Modena model, the mapping is unique, which can be readily shown with (3). The expansion with spherical harmonics on an equienergy surface is performed by the following operation,

$$\frac{1}{(2\pi)^3}\int\delta[\varepsilon-\varepsilon^\nu]Y_{l,m}(\vartheta,\varphi)\{BE\}d^3k, \tag{9}$$

where $Y_{l,m}$ is a spherical harmonic [50]. The balance equation derived from the BE by the above projection reads [29]

$$\begin{aligned}&\frac{\partial}{\partial t}\left(Z(\varepsilon)f_{l,m}(\boldsymbol{r},\varepsilon,t)\right)+\sum_{l',m'}L_{l,m,l',m'}f_{l',m'}(\boldsymbol{r},\varepsilon,t)\\&\quad+\sum_{l',m'}\Lambda_{l,m,l',m'}f_{l',m'}(\boldsymbol{r},\varepsilon,t)-\check{W}_{l,m}\{f\}(\boldsymbol{r},\varepsilon)=0,\end{aligned} \tag{10}$$

where $f_{l,m}^\nu(\boldsymbol{r},\varepsilon)$ is the expansion of $f^\nu(\boldsymbol{r},\varepsilon,\vartheta,\varphi)$,

$$f_{l,m}^\nu(\boldsymbol{r},\varepsilon)=\oint f^\nu(\boldsymbol{r},\varepsilon,\vartheta,\varphi)Y_{l,m}(\vartheta,\varphi)d\Omega. \tag{11}$$

The density-of-states $Z(\varepsilon)$ for one spin direction, which is by a factor of 4π smaller than the conventional expression, is given by

$$Z(\varepsilon)=\frac{k^2}{(2\pi)^3}\frac{\partial k}{\partial\varepsilon}. \tag{12}$$

Also we have the following relation between the magnitude of the velocity vector and the density-of-states:

$$\frac{\partial v(\varepsilon)Z(\varepsilon)}{\partial\varepsilon}=2\frac{Z(\varepsilon)}{\hbar k(\varepsilon)}. \tag{13}$$

The free steaming operator $L_{l,m,l',m'}$ in (10), which describes the effect of the electric force, is given by

$$\begin{aligned}&L_{l,m,l',m'}f_{l',m'}(\boldsymbol{r},\varepsilon)\\&=\sum_{d=1}^{3}\frac{\partial}{\partial x_d}\left[T_d^\nu a_{l,m,l',m',d}v(\varepsilon)Z(\varepsilon)f_{l',m'}(\boldsymbol{r},\varepsilon)\right]\\&\quad+F_{E,d}(\boldsymbol{r})\frac{\partial}{\partial\varepsilon}\left[T_d^\nu a_{l,m,l',m',d}v(\varepsilon)Z(\varepsilon)f_{l',m'}(\boldsymbol{r},\varepsilon)\right]\\&\quad-F_{E,d}(\boldsymbol{r})T_d^\nu b_{l,m,l',m',d}\frac{1}{\hbar k(\varepsilon)}Z(\varepsilon)f_{l',m'}(\boldsymbol{r},\varepsilon),\end{aligned} \tag{14}$$

where d (= 1, 2, and 3) is the index for the real space axis and the subscript $_d$ represents the components for the x_d direction. The free streaming operator only couples the odd part of f into the even one and vice versa. The coefficient vectors $\boldsymbol{a}_{l,m,l',m'}$ and $\boldsymbol{b}_{l,m,l',m'}$ are defined as

$$\boldsymbol{a}_{l,m,l',m'}=\oint\boldsymbol{e}_\varepsilon Y_{l,m}Y_{l',m'}d\Omega, \tag{15}$$

$$\boldsymbol{b}_{l,m,l',m'}=\oint\left(\frac{\partial Y_{l,m}}{\partial\vartheta}\boldsymbol{e}_\vartheta+\frac{1}{\sin\vartheta}\frac{\partial Y_{l,m}}{\partial\varphi}\boldsymbol{e}_\varphi\right)Y_{l',m'}d\Omega, \tag{16}$$

respectively. By their definition, we have the following relations for $\boldsymbol{a}_{l,m,l',m'}$ and $\boldsymbol{b}_{l,m,l',m'}$.

$$\boldsymbol{a}_{l,m,l',m'} = \boldsymbol{a}_{l',m',l,m}, \tag{17}$$

$$\boldsymbol{a}_{l,m,l',m'} + \boldsymbol{a}_{l',m',l,m} = \boldsymbol{b}_{l,m,l',m'} + \boldsymbol{b}_{l',m',l,m}, \tag{18}$$

$$\boldsymbol{b}_{0,0,l',m'} = 0. \tag{19}$$

The magnetic operator $\Lambda_{l,m,l',m'}$ in (10), which describes the effect of the magnetic force, is given by

$$\Lambda_{l,m,l',m'} f_{l',m'}(\boldsymbol{r},\varepsilon) = \sum_{d=1}^{3} q v(\varepsilon) \grave{B}_d^{\nu} c_{l,m,l',m',d} \frac{1}{\hbar k(\varepsilon)} Z(\varepsilon) f_{l',m'}(\boldsymbol{r},\varepsilon). \tag{20}$$

The coefficient $c_{l,m,l',m',d}$ is defined as

$$c_{l,m,l',m',d} = \oint (\boldsymbol{e}_\varepsilon \times \boldsymbol{e}_d) \cdot \left(\frac{\partial Y_{l,m}}{\partial \vartheta} \boldsymbol{e}_\vartheta + \frac{1}{\sin\vartheta} \frac{\partial Y_{l,m}}{\partial \varphi} \boldsymbol{e}_\varphi \right) Y_{l',m'} d\Omega, \tag{21}$$

where $\boldsymbol{e}_d$ is the unit vector of the Cartesian coordinate system for the x_d direction. Compared with $a_{l,m,l',m',d}$ or $b_{l,m,l',m',d}$, $c_{l,m,l',m',d}$ contains one more unit vector in its definition. Therefore, it only couples the odd(/even) part of f into the odd(/even) one.

Scattering processes with transition rates of the following form are considered

$$\check{W}_\eta^{\nu,\nu'}(\boldsymbol{r},\boldsymbol{k},\boldsymbol{k}') = \frac{1}{\Omega_s} c_\eta^{\nu,\nu'}[\boldsymbol{r},\varepsilon(\boldsymbol{k}),\cos\angle(\boldsymbol{k},\boldsymbol{k}')] \times \delta(\varepsilon(\boldsymbol{k}) - \varepsilon(\boldsymbol{k}') - \hbar\omega_\eta). \tag{22}$$

$\angle(\boldsymbol{k},\boldsymbol{k}')$ is the angle between the initial ($\boldsymbol{k}'$) and final ($\boldsymbol{k}$) wave vectors, $\hbar\omega_\eta$ the constant energy transfer and Ω_s the system volume. Neglecting the Pauli principle, the scattering integral expanded with spherical harmonics reads [29, 32, 48]

$$\check{W}_{l,m}\{f\} = \sum_{\eta,\nu'} \Big\{ Z(\varepsilon) Z(\varepsilon - \hbar\omega) c_{\eta l}^{\nu,\nu'} f_{l,m}(\boldsymbol{r},\varepsilon - \hbar\omega, t) - Z(\varepsilon + \hbar\omega) Z(\varepsilon) c_{\eta 0}^{\nu',\nu} f_{l,m}(\boldsymbol{r},\varepsilon,t) \Big\}, \tag{23}$$

where $c_{\eta,l}^{\nu,\nu'}$ is the projection of $c_\eta^{\nu,\nu'}$ onto the lth Legendre polynomial.

2.2 H-transformation

As shown in the previous subsection, the magnetic operator $\Lambda_{l,m,l',m'}$ does not contain partial derivatives. Therefore, it can be easily treated as an operator local in both real space and energy. The scattering integral $\check{W}_{l,m}$ is also local in real space. Since the stabilization is mainly concerned about the coupling between the spatial derivative and derivatives along other variables, the terms local in real space can be treated easily. Therefore, in the following discussion, we concentrate on the free steaming operator $L_{l,m,l',m'}$, which is nonlocal in real space.

In the case where the energy dependence of the distribution function is resolved by an expansion with polynomials [23], the free streaming operator includes only the partial derivative with respect to position. When we have only one partial derivative in the free-streaming operator, a stabilization scheme can be applied easily. However, since the energy is discretized with a grid in this work, we have two distinct partial derivatives with respect to either position or energy. This can cause numerical problems. To overcome these difficulties, we use the H-transformation [33]. We introduce a variable transformation from $(\boldsymbol{r},\varepsilon)$ to $(\tilde{\boldsymbol{r}},H)$:

$$\tilde{\boldsymbol{r}} = \boldsymbol{r}, \tag{24}$$

$$H = \varepsilon - q\Psi(\boldsymbol{r}), \tag{25}$$

where $\Psi(\boldsymbol{r})$ can be an arbitrary function of $\boldsymbol{r}$. According to this variable transformation, the free streaming operator is transformed as follows:

$$\begin{aligned} L_{l,m,l',m'} f_{l',m'}(\boldsymbol{r},\varepsilon) &= \tilde{L}_{l,m,l',m'} \tilde{f}_{l',m'}(\tilde{\boldsymbol{r}},H) \\ &= \sum_{d=1}^{3} \frac{\partial}{\partial \tilde{x}_d} \Big[T_d^{\nu} a_{l,m,l',m',d} \tilde{v}(\tilde{\boldsymbol{r}},H) \tilde{Z}(\tilde{\boldsymbol{r}},H) \tilde{f}_{l',m'}(\tilde{\boldsymbol{r}},H) \Big] \\ &\quad + \left(F_{E,d}(\tilde{\boldsymbol{r}}) + \frac{\partial H}{\partial x_d} \right) \\ &\quad \times \frac{\partial}{\partial H} \Big[T_d^{\nu} a_{l,m,l',m',d} \tilde{v}(\tilde{\boldsymbol{r}},H) \tilde{Z}(\tilde{\boldsymbol{r}},H) \tilde{f}_{l',m'}(\tilde{\boldsymbol{r}},H) \Big] \\ &\quad - F_{E,d}(\tilde{\boldsymbol{r}}) T_d^{\nu} b_{l,m,l',m',d} \frac{\tilde{Z}(\tilde{\boldsymbol{r}},H)}{\hbar \tilde{k}(\tilde{\boldsymbol{r}},H)} \tilde{f}_{l',m'}(\tilde{\boldsymbol{r}},H). \end{aligned} \tag{26}$$

Usually, H is identified with the total energy, therefore, the condition $\Psi(\boldsymbol{r}) = \psi(\boldsymbol{r}) - E_c^{\nu}(\boldsymbol{r})/q$ is imposed. In this case, with help of the relation

$$F_{E,d}(\boldsymbol{r}) = \frac{\partial}{\partial x_d} \left(-E_c^{\nu}(\boldsymbol{r}) + q\psi(\boldsymbol{r}) \right), \tag{27}$$

(26) reduces to

$$\begin{aligned} L_{l,m,l',m'} f_{l',m'}(\boldsymbol{r},\varepsilon) &= \tilde{L}_{l,m,l',m'} \tilde{f}_{l',m'}(\tilde{\boldsymbol{r}},H) \\ &= \sum_{d=1}^{3} \frac{\partial}{\partial \tilde{x}_d} \Big[T_d^{\nu} a_{l,m,l',m',d} \tilde{v}(\tilde{\boldsymbol{r}},H) \tilde{Z}(\tilde{\boldsymbol{r}},H) \tilde{f}_{l',m'}(\tilde{\boldsymbol{r}},H) \Big] \end{aligned}$$

$$- F_{E,d}(\tilde{\boldsymbol{r}}) T_d^v b_{l,m,l',m',d} \frac{\tilde{Z}(\tilde{\boldsymbol{r}}, H)}{\hbar \tilde{k}(\tilde{\boldsymbol{r}}, H)} \tilde{f}_{l',m'}(\tilde{\boldsymbol{r}}, H). \quad (28)$$

In this form, the free streaming operator contains only differentials with respect to position x_d. One obvious strength of the H-transformation over the discretization scheme based on the kinetic energy [29] is that the free streaming operator can be treated correctly even in the ballistic limit [51]. Of course, this advantage becomes only possible at the cost of a potential-dependent energy grid.

Since the set of equations in (10) for a given H constitutes a system of hyperbolic conservation laws, in principle, any numerical method suitable for hyperbolic systems would be applicable [23]. When the spherical harmonics expansion is restricted to the first order [33], a specific second-order differential equation for the zeroth-order component can be found. Its discretization can be done easily because a self-adjoint differential operator is involved [37]. However, the higher-order expansion in the case of a device simulation is more difficult. For example, in [38] an upwind discretization is applied to the kinetic-energy-based formula. In [29], the maximum entropy dissipation scheme [23] is directly applied to the kinetic-energy-based formulation. As discussed already, the kinetic-energy-based formula introduces an artificial broadening of electron distribution in the ballistic limit. In this work, the maximum entropy dissipation scheme is applied in addition to the H-transformation.

2.3 Maximum entropy dissipation scheme

The even part of the electron distribution function yields densities like the electron density or the energy density. In this sense the even components of the electron distribution function can be viewed as densities. Since the odd part yields the current density, the odd components can be viewed as fluxes, for which the balance equations have to be stabilized [23]. In the following, the free streaming operator which couples the odd part into the even one is labeled "even", while the opposite one is the "odd" operator.

If the entropy, which is defined as a convex function of the electron distribution function, is dissipated by the Boltzmann equation, it guarantees that the Boltzmann equation is well posed [23]. The name "maximum entropy dissipation scheme" implies that the semi-discretized system is built in such a way that it preserves this property for a specific form of the entropy function. Under the choice of the simplest possible entropy function, $\frac{1}{2}\exp(\frac{H}{k_B T_0}) f^2$ [23], the free streaming operator is a skew self adjoint operator under the weight function $\exp(\frac{H}{k_B T_0})$. $k_B T_0$ is the thermal energy evaluated at the lattice temperature T_0. Therefore, in the maximum entropy dissipation scheme, the odd operator is expressed as the negative adjoint form of the corresponding even operator with the weighting factor.

When we apply this scheme to the kinetic-energy-based formula directly, this weighting factor plays an important role, because it is a function of position. However, in the case of the total-energy-based formula, it is just a constant, therefore, we can simply take the negative adjoint operator. Following this scheme, the odd operator $\tilde{L}_{l',m',l,m}$ (l' is odd and l even.) is given by

$$\begin{aligned}
&\tilde{L}_{l',m',l,m} \tilde{f}_{l,m}(\tilde{\boldsymbol{r}}, H) \\
&\quad = \sum_{d=1}^{3} T_d^v a_{l,m,l',m',d} \tilde{v}(\tilde{\boldsymbol{r}}, H) \tilde{Z}(\tilde{\boldsymbol{r}}, H) \frac{\partial}{\partial \tilde{x}_d} \tilde{f}_{l,m}(\tilde{\boldsymbol{r}}, H) \\
&\qquad + F_{E,d}(\tilde{\boldsymbol{r}}) T_d^v b_{l,m,l',m',d} \frac{\tilde{Z}(\tilde{\boldsymbol{r}}, H)}{\hbar \tilde{k}(\tilde{\boldsymbol{r}}, H)} \tilde{f}_{l,m}(\tilde{\boldsymbol{r}}, H). \quad (29)
\end{aligned}$$

Note that the index pairs (l, m) and (l', m') are interchanged in the coefficients of the equation. Equivalence of this form and its original form can be easily shown by (13), (17), and (18).

Let us have a look at $\tilde{L}_{0,0,1,m'} \tilde{L}_{1,m',0,0} \tilde{f}_{0,0}(\tilde{\boldsymbol{r}}, H)$, which is obtained, when the first order equation is inserted into the zeroth order equation. Besides the inverse scattering operator for $\tilde{f}_{1,m'}(\tilde{\boldsymbol{r}}, H)$, it corresponds to the free streaming operator for $\tilde{f}_{0,0}(\tilde{\boldsymbol{r}}, H)$. Using the expressions for both $\tilde{L}_{1,m',0,0}$ and $\tilde{L}_{0,0,1,m'}$, (19), and the property $a_{0,0,1,m',d} a_{0,0,1,m',d'} = 0$ when $d \neq d'$, we have

$$\begin{aligned}
&\tilde{L}_{0,0,1,m'} \tilde{L}_{1,m',0,0} \tilde{f}_{0,0}(\tilde{\boldsymbol{r}}, H) \\
&\quad = \sum_{d=1}^{3} (T_d^v a_{0,0,1,m'})^2 \\
&\qquad \times \frac{\partial}{\partial \tilde{x}_d} \left[\tilde{v}^2(\tilde{\boldsymbol{r}}, H) \tilde{Z}^2(\tilde{\boldsymbol{r}}, H) \frac{\partial}{\partial \tilde{x}_d} \tilde{f}_{0,0}(\tilde{\boldsymbol{r}}, H) \right]. \quad (30)
\end{aligned}$$

Together with the scattering operator, this ensures that the Jacobian matrix for $\tilde{f}_{0,0}(\tilde{\boldsymbol{r}}, H)$ has property M [52].

The balance equation after the stabilization, which is a partial differential equation over the two-dimensional real space, is discretized by the box integration method [53]. It is integrated over the control volume in the three-dimensional energy/real space.

For box integration a special grid for the real space is introduced. Figure 1 shows a part of the two-dimensional real space grid. The electron distribution function $\tilde{f}_{l,m}$ with even l is defined on the direct grid nodes (filled circles). The box G^{i_v} for the direct grid node i_v contains all points which are closest to the grid node i_v. For the electron distribution function with odd l, adjoint nodes are assigned, which are given by the nodes on the midpoint between two neighboring direct nodes. In Fig. 1, the adjoint nodes are denoted as opened circles. Dimensional splitting along the lines between two neighboring direct nodes (solid lines) is employed for the odd operator.

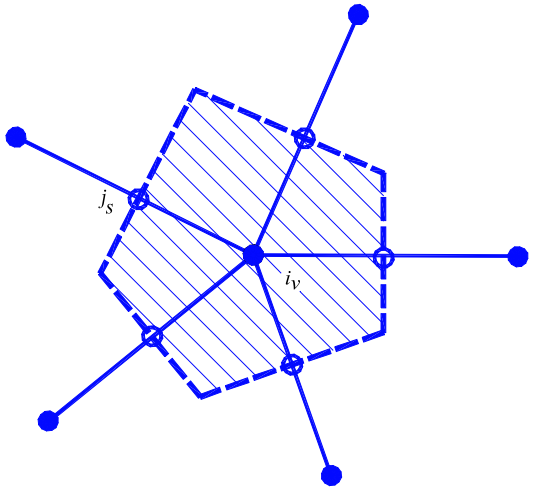

Fig. 1 Direct nodes (*filled circles*) and adjoint nodes (*open circles*)

In the following, a Cartesian tensor grid for the real space is assumed for the sake of brevity, however, its extension to unstructured grids is straightforward. By an integer subscript we denote the direct grid points. The adjoint point between two adjacent direct grid points is denoted by the subscript whose value is the average of the two subscripts. For example, $\tilde{x}_{i+0.5}$ denotes the adjoint point between $\tilde{x}_i$ and $\tilde{x}_{i+1}$.

In the case of the energy space, a uniform grid is employed. Since the uniform energy grid is shared by all valleys, intervalley scattering can be treated easily even when the valley minimum is shifted from the conduction band edge due to the position-dependent Ge content [44]. The total energy range for a given n-th energy point, whose H value is H_n, is denoted by (H_n^-, H_n^+). If the valley minimum is located within this range, the integral over the energy space is valid only from that value, not from H_n^-. The minimum value of the valid total energy for the given n-th energy range is denoted by $H_n^{min}(\tilde{x})$. Then $H_n^{min}(\tilde{x})$ can be obtained by

$$H_n^{min}(\tilde{x}) = \min\{H_n^+, \max\{H_n^-, E_c^v(x) - q\psi(\tilde{x})\}\}. \tag{31}$$

Note that $H_n^{min}(\tilde{x})$ may depend on the electrostatic potential.

First, the discretization of the odd free streaming operator is shown. Since the dimensional splitting is employed for the odd operator, we may consider only one spatial derivative along the direction of the line on which the adjoint node is located, let's say $\tilde{x}$.

$$\begin{aligned}
&\tilde{L}_{l',m',l,m}\tilde{f}_{l,m}(\tilde{x}, H) \\
&\quad = T^v_{\tilde{x}} a_{l,m,l',m',\tilde{x}} \tilde{v}(\tilde{x}, H)\tilde{Z}(\tilde{x}, H)\frac{\partial}{\partial \tilde{x}}\tilde{f}_{l,m}(\tilde{x}, H) \\
&\qquad + F_{E,\tilde{x}}(\tilde{x}) T^v_{\tilde{x}} b_{l,m,l',m',\tilde{x}} \frac{\tilde{Z}(\tilde{x}, H)}{\hbar\tilde{k}(\tilde{x}, H)}\tilde{f}_{l,m}(\tilde{x}, H).
\end{aligned} \tag{32}$$

The odd components can be viewed as fluxes. Therefore, the odd component is defined only when the two surrounding direct nodes have non-vanishing integrated density-of-states over the control volume. The odd operator is integrated over $\tilde{x}$ (from $\tilde{x}_i$ to $\tilde{x}_{i+1}$) and H (from H_n^- to H_n^+),

$$\begin{aligned}
&\int_{H_n^-}^{H_n^+}\int_{\tilde{x}_i}^{\tilde{x}_{i+1}} \tilde{L}_{l',m',l,m}\tilde{f}_{l,m}(\tilde{x}, H)d\tilde{x}dH \\
&\quad = T^v_{\tilde{x}} a_{l,m,l',m',\tilde{x}} \int_{H_n^-}^{H_n^+} \tilde{v}(\tilde{x}_{i+0.5}, H)\tilde{Z}(\tilde{x}_{i+0.5}, H)dH \\
&\qquad \times \left[\tilde{f}_{l,m}(\tilde{x}_{i+1}, H_n) - \tilde{f}_{l,m}(\tilde{x}_i, H_n)\right] \\
&\qquad + F_{E,\tilde{x}}(\tilde{x}_{i+0.5}) T^v_{\tilde{x}} b_{l,m,l',m',\tilde{x}} \int_{H_n^-}^{H_n^+} \frac{\tilde{Z}(\tilde{x}_{i+0.5}, H)}{\hbar\tilde{k}(\tilde{x}_{i+0.5}, H)}dH \\
&\qquad \times \left[\tilde{f}_{l,m}(\tilde{x}_i, H_n)\frac{\tilde{x}_{i+1} - \tilde{x}_i}{2}\right] \\
&\qquad + F_{E,\tilde{x}}(\tilde{x}_{i+0.5}) T^v_{\tilde{x}} b_{l,m,l',m',\tilde{x}} \int_{H_n^-}^{H_n^+} \frac{\tilde{Z}(\tilde{x}_{i+0.5}, H)}{\hbar\tilde{k}(\tilde{x}_{i+0.5}, H)}dH \\
&\qquad \times \left[\tilde{f}_{l,m}(\tilde{x}_{i+1}, H_n)\frac{\tilde{x}_{i+1} - \tilde{x}_i}{2}\right].
\end{aligned} \tag{33}$$

For the Modena model, we can derive analytical expressions for the integrals in the above equation

$$\begin{aligned}
&\int_{H_n^-}^{H_n^+} \tilde{v}(\tilde{x}_{i+0.5}, H)\tilde{Z}(\tilde{x}_{i+0.5}, H)dH \\
&\quad = \frac{2m_d}{(2\pi\hbar)^3}\left[\frac{1}{2}(H_n^+ - E_c^v(\tilde{x}_{i+0.5}) + q\psi(\tilde{x}_{i+0.5}))^2\right. \\
&\qquad - \frac{1}{2}(H_n^{min}(\tilde{x}_{i+0.5}) - E_c^v(\tilde{x}_{i+0.5}) + q\psi(\tilde{x}_{i+0.5}))^2 \\
&\qquad + \frac{\alpha}{3}(H_n^+ - E_c^v(\tilde{x}_{i+0.5}) + q\psi(\tilde{x}_{i+0.5}))^3 \\
&\qquad \left. - \frac{\alpha}{3}(H_n^{min}(\tilde{x}_{i+0.5}) - E_c^v(\tilde{x}_{i+0.5}) + q\psi(\tilde{x}_{i+0.5}))^3\right],
\end{aligned} \tag{34}$$

$$\begin{aligned}
&\int_{H_n^-}^{H_n^+} \frac{\tilde{Z}(\tilde{x}_{i+0.5}, H)}{\hbar\tilde{k}(\tilde{x}_{i+0.5}, H)}dH \\
&\quad = \frac{m_d}{(2\pi\hbar)^3}\left[(H_n^+ - E_c^v(\tilde{x}_{i+0.5}) + q\psi(\tilde{x}_{i+0.5}))\right. \\
&\qquad - (H_n^{min}(\tilde{x}_{i+0.5}) - E_c^v(\tilde{x}_{i+0.5}) + q\psi(\tilde{x}_{i+0.5})) \\
&\qquad + \alpha(H_n^+ - E_c^v(\tilde{x}_{i+0.5}) + q\psi(\tilde{x}_{i+0.5}))^2 \\
&\qquad \left. - \alpha(H_n^{min}(\tilde{x}_{i+0.5}) - E_c^v(\tilde{x}_{i+0.5}) + q\psi(\tilde{x}_{i+0.5}))^2\right].
\end{aligned} \tag{35}$$

Therefore, the dependence of these analytical expressions on $\psi(\tilde{x}_i)$ and $\psi(\tilde{x}_{i+1})$ can be obtained. Note that both,

the direct dependence on $\psi(\tilde{x}_i)$ and $\psi(\tilde{x}_{i+1})$ and the dependence through $H_n^{min}(\tilde{x})$ should be considered.

Next, the discretization of the even free streaming operator is shown. Since we employ dimensional splitting for the odd operator, we have four adjoint nodes surrounding the given direct node. For example, let us assume that the direct node is given by $\tilde{x}_i$ and $\tilde{y}_j$. The surrounding four adjoint nodes are $\tilde{x}_{i\pm0.5}$ and $\tilde{y}_{j\pm0.5}$. Explicitly in the two-dimensional real space,

$$\begin{aligned}
&\tilde{L}_{l,m,l',m'}\tilde{f}_{l',m'}(\tilde{\boldsymbol{r}},H)\\
&\quad=\frac{\partial}{\partial\tilde{x}}\Big[T^v_{\tilde{x}}a_{l,m,l',m',\tilde{x}}\tilde{v}(\tilde{\boldsymbol{r}},H)\tilde{Z}(\tilde{\boldsymbol{r}},H)\tilde{f}_{l',m'}(\tilde{\boldsymbol{r}},H)\Big]\\
&\qquad-F_{E,\tilde{x}}(\tilde{\boldsymbol{r}})T^v_{\tilde{x}}b_{l,m,l',m',\tilde{x}}\frac{\tilde{Z}(\tilde{\boldsymbol{r}},H)}{\hbar\tilde{k}(\tilde{\boldsymbol{r}},H)}\tilde{f}_{l',m'}(\tilde{\boldsymbol{r}},H)\\
&\qquad+\frac{\partial}{\partial\tilde{y}}\Big[T^v_{\tilde{y}}a_{l,m,l',m',\tilde{y}}\tilde{v}(\tilde{\boldsymbol{r}},H)\tilde{Z}(\tilde{\boldsymbol{r}},H)\tilde{f}_{l',m'}(\tilde{\boldsymbol{r}},H)\Big]\\
&\qquad-F_{E,\tilde{y}}(\tilde{\boldsymbol{r}})T^v_{\tilde{y}}b_{l,m,l',m',\tilde{y}}\frac{\tilde{Z}(\tilde{\boldsymbol{r}},H)}{\hbar\tilde{k}(\tilde{\boldsymbol{r}},H)}\tilde{f}_{l',m'}(\tilde{\boldsymbol{r}},H). \qquad (36)
\end{aligned}$$

Defining the even operator along $\tilde{x}$-direction as follows,

$$\begin{aligned}
&\tilde{L}_{l,m,l',m',\tilde{x}}\tilde{f}_{l',m'}(\tilde{\boldsymbol{r}},H)\\
&\quad=\frac{\partial}{\partial\tilde{x}}\Big[T^v_{\tilde{x}}a_{l,m,l',m',\tilde{x}}\tilde{v}(\tilde{\boldsymbol{r}},H)\tilde{Z}(\tilde{\boldsymbol{r}},H)\tilde{f}_{l',m'}(\tilde{\boldsymbol{r}},H)\Big]\\
&\qquad-F_{E,\tilde{x}}(\tilde{\boldsymbol{r}})T^v_{\tilde{x}}b_{l,m,l',m',\tilde{x}}\frac{\tilde{Z}(\tilde{\boldsymbol{r}},H)}{\hbar\tilde{k}(\tilde{\boldsymbol{r}},H)}\tilde{f}_{l',m'}(\tilde{\boldsymbol{r}},H), \qquad (37)
\end{aligned}$$

and the one along $\tilde{y}$-direction in the same manner, we can treat the contributions from the specific directions separately. When the grid node is located on the interface of silicon and oxide regions, only (the part of) the area which lies inside the silicon region is considered. Without loss of generality, let us consider $\tilde{L}_{l,m,l',m',\tilde{x}}\ \tilde{f}_{l',m'}(\tilde{\boldsymbol{r}},H)$ only. The integral of the even operator over $\tilde{x}$ (from $\tilde{x}_{i-0.5}$ to $\tilde{x}_{i+0.5}$) and H (from H_n^- to H_n^+) is considered.

$$\begin{aligned}
&\int_{H_n^-}^{H_n^+}\int_{\tilde{x}_{i-0.5}}^{\tilde{x}_{i+0.5}}\tilde{L}_{l,m,l',m',\tilde{x}}\tilde{f}_{l',m'}(\tilde{\boldsymbol{r}},H)d\tilde{x}dH\\
&\quad=T^v_{\tilde{x}}a_{l,m,l',m',\tilde{x}}\int_{H_n^-}^{H_n^+}\tilde{v}(\tilde{x}_{i+0.5},H)\tilde{Z}(\tilde{x}_{i+0.5},H)dH\\
&\qquad\times\tilde{f}_{l',m'}(\tilde{x}_{i+0.5},H_n)\\
&\qquad-T^v_{\tilde{x}}a_{l,m,l',m',\tilde{x}}\int_{H_n^-}^{H_n^+}\tilde{v}(\tilde{x}_{i-0.5},H)\tilde{Z}(\tilde{x}_{i-0.5},H)dH\\
&\qquad\times\tilde{f}_{l',m'}(\tilde{x}_{i-0.5},H_n)\\
&\qquad-F_{\tilde{x}}(\tilde{x}_{i-0.5})T^v_{\tilde{x}}b_{l,m,l',m',\tilde{x}}\int_{H_n^-}^{H_n^+}\frac{\tilde{Z}(\tilde{x}_{i-0.5},H)}{\hbar\tilde{k}(\tilde{x}_{i-0.5},H)}dH\\
&\qquad\times\Big[\tilde{f}_{l',m'}(\tilde{x}_{i-0.5},H_0)\frac{\tilde{x}_i-\tilde{x}_{i-1}}{2}\Big]\\
&\qquad-F_{\tilde{x}}(\tilde{x}_{i+0.5})T^v_{\tilde{x}}b_{l,m,l',m',\tilde{x}}\int_{H_n^-}^{H_n^+}\frac{\tilde{Z}(\tilde{x}_{i+0.5},H)}{\hbar\tilde{k}(\tilde{x}_{i+0.5},H)}dH\\
&\qquad\times\Big[\tilde{f}_{l',m'}(\tilde{x}_{i+0.5},H_0)\frac{\tilde{x}_{i+1}-\tilde{x}_i}{2}\Big], \qquad (38)
\end{aligned}$$

where the coefficients are already defined in (34) and (35).

Since the magnetic operator and the scattering integral are local in real space, their discretization is performed without much difficulty. Note that the dependence of $c^{v,v'}_{\eta,l}$ on the electrostatic potential also should be considered.

2.4 Boundary condition

For all equations considered in this work (the Poisson equation, the Boltzmann equation, and the hole continuity equation), the Neumann boundary condition is imposed on a non-contact boundary. For the Poisson equation and the hole continuity equation, the Dirichlet boundary condition is imposed on a contact boundary.

In the case of the Boltzmann equation, instead of the Dirichlet boundary condition we use Neumann boundary conditions together with a surface generation rate

$$\Gamma^s(\boldsymbol{k}')=[f^{eq}(\boldsymbol{k}')\theta(\hat{T}\boldsymbol{v}\cdot\boldsymbol{n})+f(\boldsymbol{k}')\theta(-\hat{T}\boldsymbol{v}\cdot\boldsymbol{n})]\hat{T}\boldsymbol{v}\cdot\boldsymbol{n}, \quad (39)$$

where $\boldsymbol{n}$ is a surface vector pointing into the device, $\theta(x)$ the step function and f^{eq} the equilibrium distribution specified by the electron quasi-Fermi level of the contact. This boundary condition corresponds to a thermal bath contact similar to the ones used in Monte Carlo simulations [54]. The injected particle flux (the first term on the right hand side) is the result of an equilibrium distribution, whereas the extracted particle flux (the second term) is due to the distribution in the device. The surface generation rate is projected onto spherical harmonics

$$\Gamma^s_{l,m}(\varepsilon)=\sum_{l',m'}Z(\varepsilon)[f_{l',m'}(\varepsilon)d_{l,m,l',m'}+f^{eq}_{l',m'}(\varepsilon)e_{l,m,l',m'}] \quad (40)$$

with

$$d_{l,m,l',m'}=\oint\theta(-\hat{T}\boldsymbol{v}\cdot\boldsymbol{n})\hat{T}\boldsymbol{v}\cdot\boldsymbol{n}Y_{l',m'}(\Omega)Y_{l,m}(\Omega)d\Omega \quad (41)$$

and

$$e_{l,m,l',m'}=\oint\theta(\hat{T}\boldsymbol{v}\cdot\boldsymbol{n})\hat{T}\boldsymbol{v}\cdot\boldsymbol{n}Y_{l',m'}(\Omega)Y_{l,m}(\Omega)d\Omega. \quad (42)$$

The surface generation rate is implemented as a volume generation rate within the box of the terminal.

2.5 Small-Signal Analysis

When the device in the steady-state is subjected to a small perturbation with angular frequency ω, the resultant electrostatic potential can be expressed in the complex domain as $\psi(\boldsymbol{r},t)=\psi_s(\boldsymbol{r})+\delta\psi(\boldsymbol{r},\omega)e^{j\omega t}$. Also the corresponding deviation of the electron distribution function at angular frequency ω is given by $\delta f(\boldsymbol{r},\varepsilon,\omega)e^{j\omega t}$. In order to avoid the numerical difficulties arising from the time-varying density-of-states, following the idea in [39], we fix $\Psi(\boldsymbol{r})$. When we set $\Psi(\boldsymbol{r})=\psi_s(\boldsymbol{r})-E_c^v(\boldsymbol{r})/q$, the linearized free streaming operators for the deviations are written in the H-transformed space,

$$\begin{aligned}&\tilde{L}_{l,m,l',m'}\tilde{\delta f}_{l',m'}(\tilde{\boldsymbol{r}},H,\omega)\\&\quad=\sum_{d=1}^{3}\frac{\partial}{\partial\tilde{x}_d}\Big[T_d^v a_{l,m,l',m',d}\tilde{v}(\tilde{\boldsymbol{r}},H)\tilde{Z}(\tilde{\boldsymbol{r}},H)\\&\qquad\times\tilde{\delta f}_{l',m'}(\tilde{\boldsymbol{r}},H,\omega)\Big]\\&\qquad-F_{E,d}(\tilde{\boldsymbol{r}})T_d^v b_{l,m,l',m',d}\frac{\tilde{Z}(\tilde{\boldsymbol{r}},H)}{\hbar\tilde{k}(\tilde{\boldsymbol{r}},H)}\tilde{\delta f}_{l',m'}(\tilde{\boldsymbol{r}},H,\omega),\end{aligned}\tag{43}$$

$$\begin{aligned}&\delta\tilde{L}_{l,m,l',m'}\tilde{f}_{s,l',m'}(\tilde{\boldsymbol{r}},H)\\&\quad=\sum_{d=1}^{3}q\frac{\partial\delta\psi(\boldsymbol{r},\omega)}{\partial x_d}\\&\qquad\times\frac{\partial}{\partial H}\Big[T_d^v a_{l,m,l',m',d}\tilde{v}(\tilde{\boldsymbol{r}},H)\tilde{Z}(\tilde{\boldsymbol{r}},H)\tilde{f}_{s,l',m'}(\tilde{\boldsymbol{r}},H)\Big],\end{aligned}\tag{44}$$

where $\tilde{f}_{s,l',m'}$ denotes the steady-state solution of $\tilde{f}_{l',m'}$. Since $\delta\psi(\boldsymbol{r},\omega)$ cannot be neglected in the small-signal analysis, the coupling between different H-points should be treated. The coefficient of $\frac{\partial\delta\psi(\boldsymbol{r},\omega)}{\partial x_d}$ is calculated by a suitable interpolation scheme. Once the coefficient is calculated and fixed, the term is linear in the potential perturbation.

Following the above procedure, the small-signal Y-parameters can be readily calculated. In the case of noise simulation, the solution of the adjoint system [55–57] is required. Once a suitable Green's function for the output variable is evaluated, the power spectral density of the fluctuations of the output variable can be calculated in the way described in [40].

3 Results

Three examples, an n^+nn^+ structure, a partially-depleted SOI MOSFET, and a SiGe HBT, are presented. The examples have been selected to demonstrate the strength of the deterministic Boltzmann equation solver. For the n^+nn^+ structure, the effect of a magnetic field on the device performance is demonstrated. For the partially-depleted SOI MOSFET, the effect of impact ionization on the device characteristic is analyzed. For the SiGe HBT, the noise performance is investigated.

All results are calculated at room temperature (300 K).

3.1 Transport in the n^+nn^+ structure

The direction of the magnetic field is assumed to be perpendicular to the two-dimensional simulation plane, $\boldsymbol{B}=B\boldsymbol{e}_z$. In this case, only $c_{l,m,l',m',z}$ has to be calculated, which is rearranged from (21) as follows,

$$\begin{aligned}&c_{l,m,l',m',z}\\&\quad=\oint\left(-\cos\vartheta\frac{\partial Y_{l,m}}{\partial\vartheta}+\frac{\cos\vartheta\sin\varphi}{\sin\vartheta}\frac{\partial Y_{l,m}}{\partial\varphi}\right)Y_{l',m'}d\Omega.\end{aligned}\tag{45}$$

The doping profile of the n^+nn^+ structure with a 40 nm long lowly doped region between two highly doped contact regions is shown in Fig. 2. The structure is assumed to be homogeneous and infinitely wide in the y-direction. A previous study of this structure [58] has shown that strong built-in fields occur in the junctions and even the linear response at equilibrium contains a ballistic part.

In Fig. 3, absolute values of the relative change of the terminal current at different applied voltages relative to 0 T are shown for two magnetic fields, 1 T and 10 T. The change due to the magnetic field is small even at a high magnetic field. For example, the biggest change in the figure is about 7% at 10 T. Therefore, it is very CPU time consuming to simulate magnetotransport with the Monte Carlo approach. The effect of the magnetic field on the terminal current is stronger

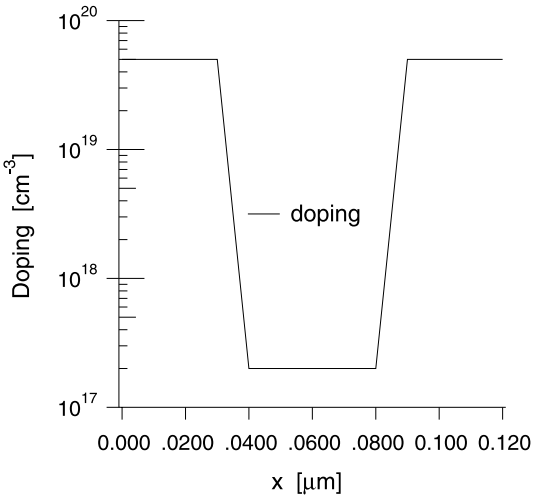

Fig. 2 Doping profile of the 40 nm n^+nn^+ structure (reprint from [31])

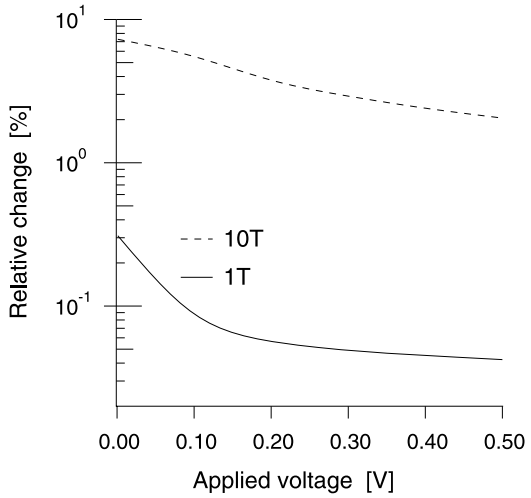

Fig. 3 Absolute values of the relative change of the simulated terminal current at different applied voltages relative to 0 T (reprint from [31])

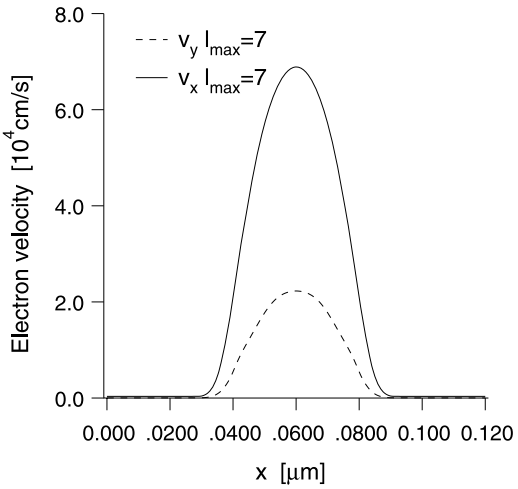

Fig. 4 Electron velocities along x- and y-directions at $V = 1$ mV and $B = 10$ T (reprint from [31])

at low applied voltage than at higher applied voltage. In Fig. 4, the electron velocities along x- and y-directions at $V = 1$ mV and $B = 10$ T are shown. The ratio of y and x-components has its peak value in the lowly doped region. In Fig. 5, the electron velocities along x- and y-directions at $V = 0.5$ V and $B = 10$ T are shown. Hot electron effects reduce the peak value of the velocity ratio compared to the result for $V = 1$ mV. It can be understood by comparing the relative magnitude of the magnetic operator with those of the free streaming operator and the scattering integral.

In Fig. 6 the electron distribution function multiplied by the density-of-states is shown in the k-space for the valley with the longitudinal mass aligned to x-axis at $V = 0.5$ V and $B = 0$ T in the middle of the device. The distribution is symmetric with respect to k_y and a ballistic peak appears at about $k_x = 0.16 \cdot 2\pi/a_0$. In Fig. 7, the same quantity at

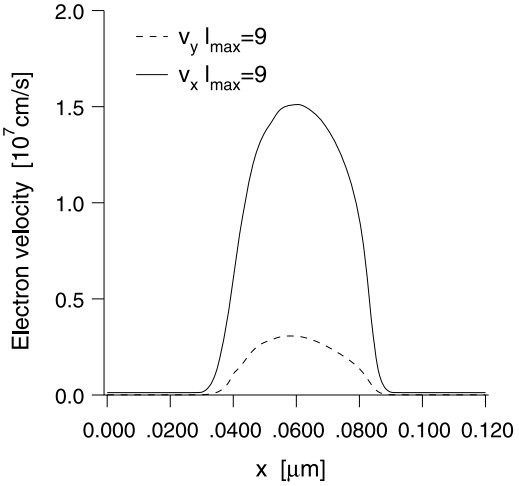

Fig. 5 Electron velocities along x- and y-directions at $V = 0.5$ V and $B = 10$ T (reprint from [31])

$B = 10$ T is shown. The distortion toward the positive k_y direction due to the magnetic force is clearly seen.

One important question regarding the spherical harmonics expansion is, whether the order of spherical harmonics is sufficiently large or not. In Fig. 8, the electron velocities along x-direction for different numbers of spherical harmonics are shown. The applied bias is 0.5 V and the magnetic field is 10 T. The convergence is clearly visible already for the third order. In Fig. 9, the electron velocities along y-direction for the same conditions are shown. It is obvious that the velocity along y-direction requires more spherical harmonics than that along x-direction, and convergence occurs for the seventh order. It can be understood by realizing the different coupling behavior of $c_{l,m,l',m',d}$, which is related with the magnetic operator, from other coefficients such as $a_{l,m,l',m',d}$ and $b_{l,m,l',m',d}$.

3.2 Partially-depleted SOI MOSFET

Numerical simulation of a partially-depleted SOI MOSFET is known to be a very challenging task [59–61]. Floating-body effects are determined by a delicate balance between various generation and recombination mechanisms (SRH generation/recombination mechanism, impact ionization, etc) and hot electron injection from the drain end of the MOSFET channel.

The quantization of carrier motion perpendicular to the interface is not taken into account. In order to account for inversion-layer transport, additional scattering mechanisms are included in the simulation [32], and the parameters for those scattering processes are matched to the CVT mobility model [62]. The impact ionization model of [63] is exploited. In this simulation, the SRH generation/recombination mechanism is not considered.

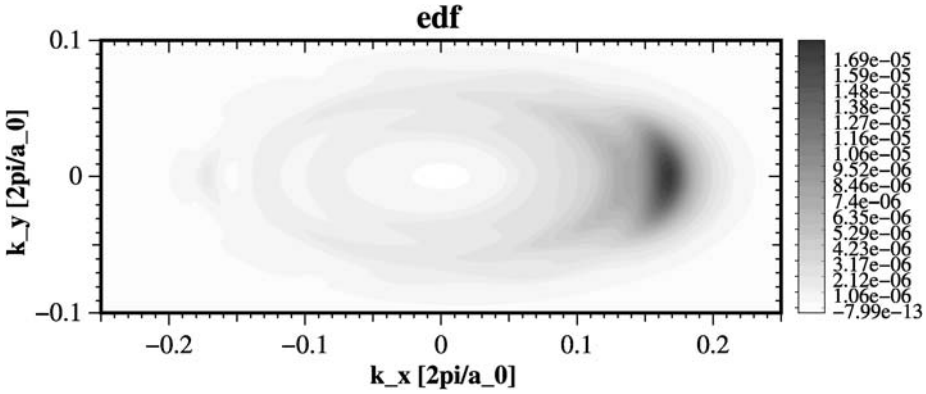

Fig. 6 Electron distribution function multiplied by the density-of-states in the valley with the longitudinal mass aligned to x-axis at $V = 0.5$ V and $B = 0$ T and $k_z = 0$ in the middle of the device (reprint from [31])

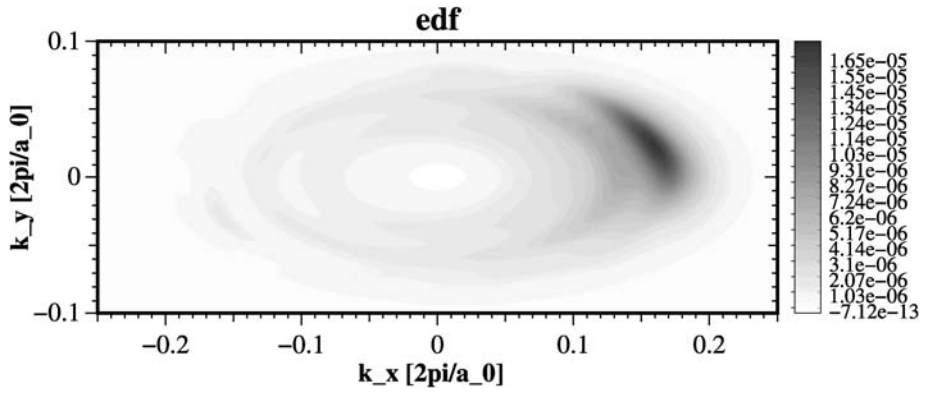

Fig. 7 Electron distribution function for the same conditions as in Fig. 6 besides a magnetic field of 10 T (reprint from [31])

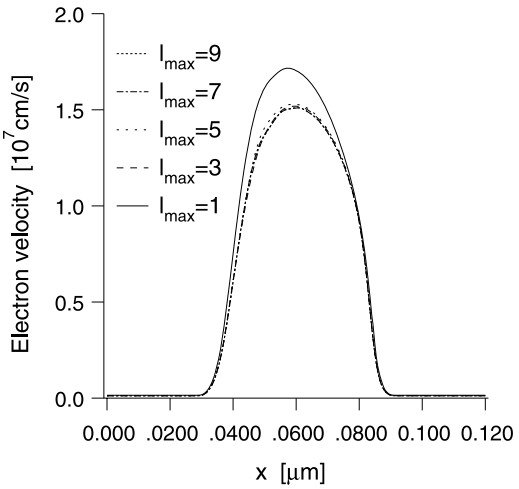

Fig. 8 Electron velocities along x-direction for different numbers of spherical harmonics at $V = 0.5$ V and $B = 10$ T (reprint from [31])

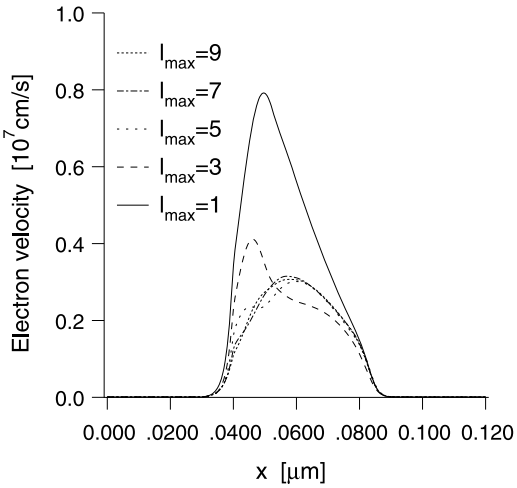

Fig. 9 Electron velocities along y-direction for different numbers of spherical harmonics at $V = 0.5$ V and $B = 10$ T (reprint from [31])

The outline of the SOI MOSFET [64] is shown in Fig. 10. The simulated SOI NMOSFET has a body thickness of 180 nm, a top oxide of 8.5 nm, a bottom oxide of 400 nm, and a gate length of 500 nm. It is discretized with a grid of 63×81 nodes with a non-uniform spacing. The device is of the partially-depleted type and has a homogeneous body doping of $2 \times 10^{17}/\text{cm}^3$.

The output characteristics of the device are shown in Fig. 11 and the kink effect is clearly visible. In Fig. 12, the corresponding source hole current generated by impact ionization is shown.

In Fig. 13 the electron concentration is shown for $V_{GS} = 1.0$ V and $V_{DS} = 1.0$ V, above the kink. It is seen that the vertical diffusion of electrons near the drain end of the MOSFET channel is not strong in contrast to hydrodynamic simulations [59, 60]. In Fig. 14 the electron dynamic temperature [65] and the impact ionization generation rate are shown along the Si/SiO_2 interface for $V_{GS} = 1.0$ V and

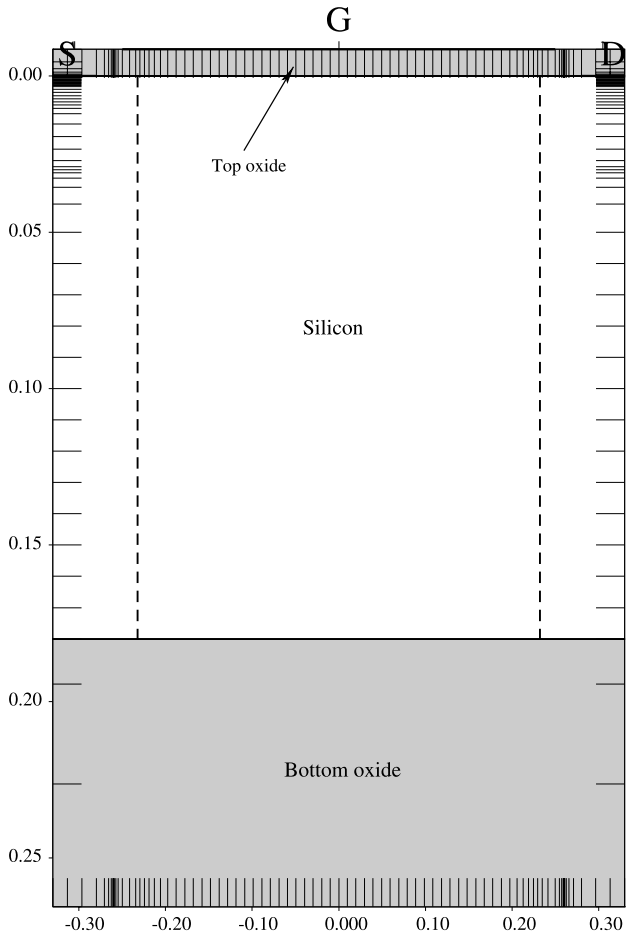

Fig. 10 2D structure of the SOI MOSFET. Only part of the bottom oxide whose thickness is 400 nm is shown. The ticks indicate the real space grid

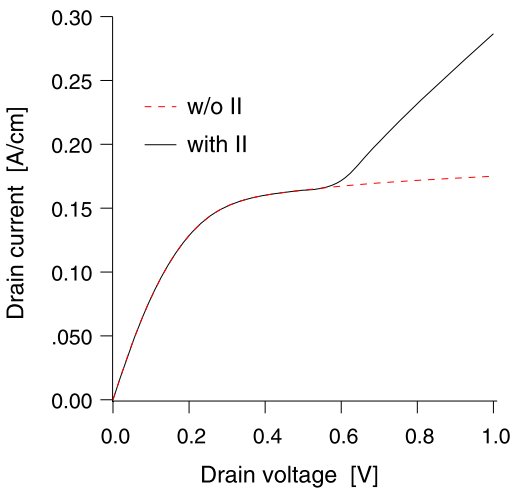

Fig. 11 Output characteristics of the SOI MOSFET for $V_{GS} = 1.0$ V with and without impact ionization

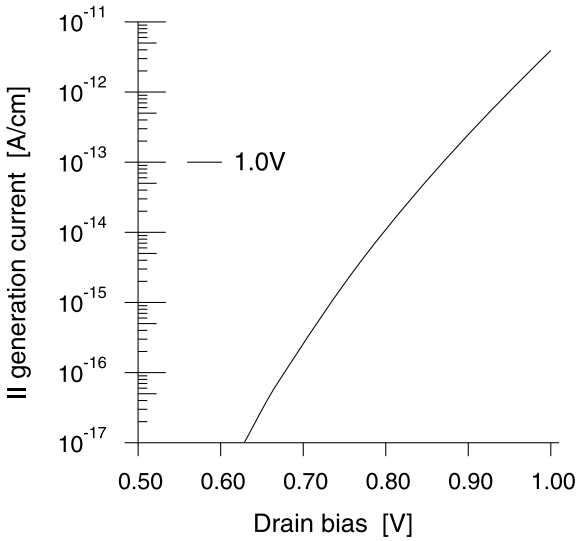

Fig. 12 Source hole current generated by impact ionization of the SOI MOSFET for $V_{GS} = 1.0$ V

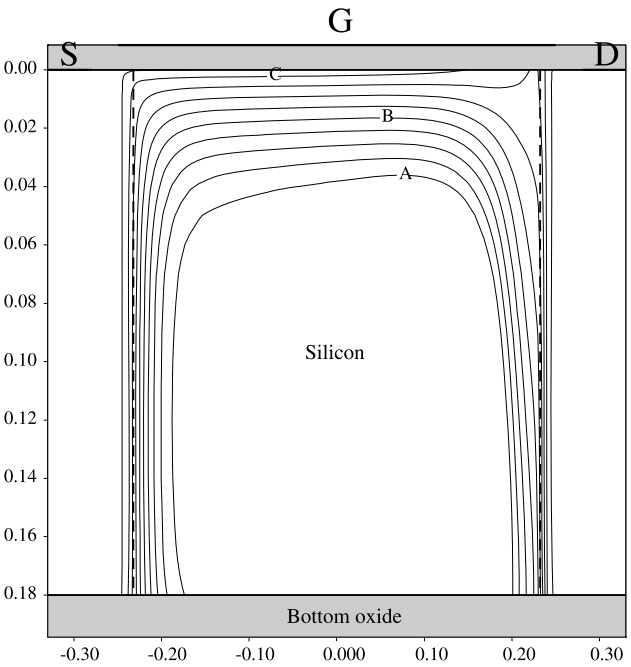

Fig. 13 Electron concentration in the SOI MOSFET for $V_{GS} = 1.0$ V and $V_{DS} = 1.0$ V. Labels A, B, and C correspond to $10^{10}/\text{cm}^3$, $10^{14}/\text{cm}^3$, and $10^{18}/\text{cm}^3$, respectively

$V_{DS} = 1.0$ V. Both quantities are rather unrelated and impact ionization cannot be described by a local temperature model typically used in hydrodynamic simulations [66]. The peak of the impact ionization generation rate appears closer to the drain contact than that of the dynamic temperature. Thus, more holes generated by impact ionization flow out through the drain terminal than a local temperature model would predict.

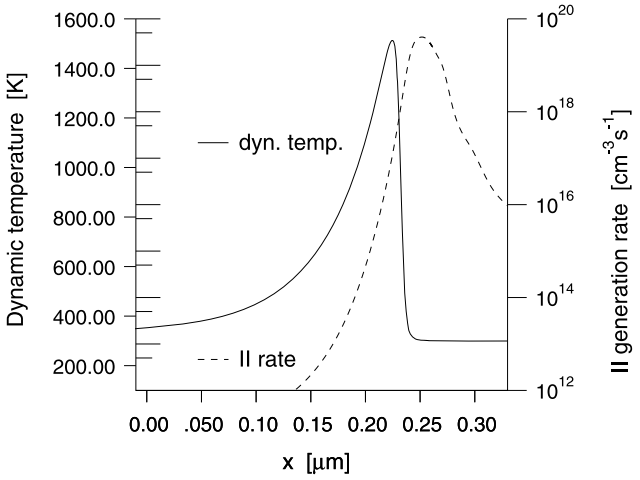

Fig. 14 Electron dynamic temperature and impact ionization generation rate along the Si/SiO_2 interface for $V_{GS} = 1.0$ V and $V_{DS} = 1.0$ V

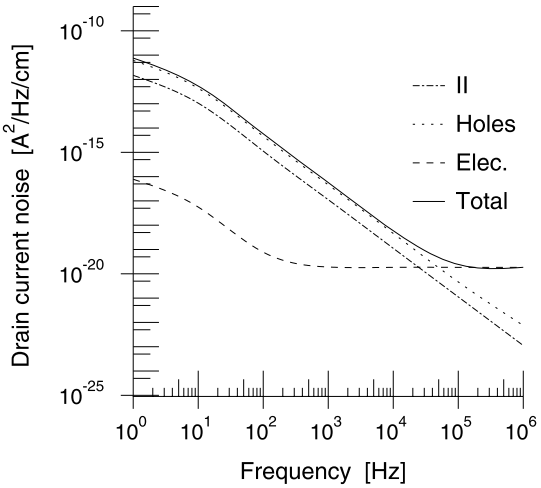

Fig. 15 Spectral intensity of the drain current fluctuations for $V_{GS} = 1.0$ V and $V_{DS} = 1.0$ V

The low frequency noise for $V_{GS} = 1.0$ V and $V_{DS} = 1.0$ V is shown in Fig. 15. The contributions of the different noise sources to the drain current noise are also shown. Above the kink, the noise is caused by impact ionization and hole scattering. Impact ionization and hole scattering both yield shot-like noise which is strongly amplified by the floating body effect [67]. At higher frequencies this feedback effect is short-circuited by capacitive coupling and the decrease in noise with frequency is similar to the effect of a low-pass filter of the first order.

3.3 SiGe HBT

The RF and noise performance of a SiGe HBT, which is pseudomorphically grown on unstrained silicon, is investigated. Apparent bandgap narrowing due to heavy doping is included [68]. Detailed comparison of the Boltzmann equation result with drift-diffusion and hydrodynamic models and discussion of the accuracy of the classical models can be found elsewhere, and will not be repeated.

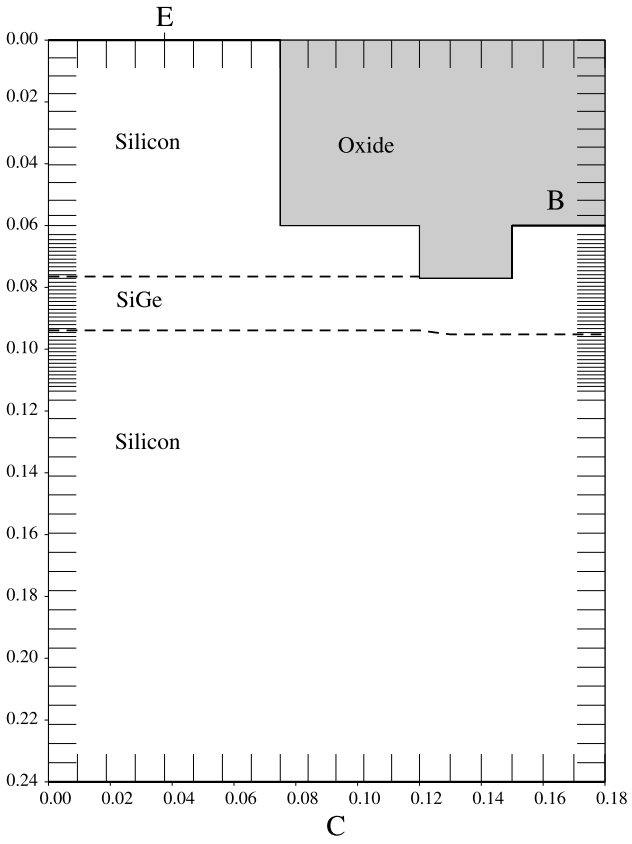

Fig. 16 2D structure of the SiGe HBT. The ticks indicate the real space grid

The outline of the simulated SiGe HBT is shown in Fig. 16. The device is symmetric to the line $y = 0$ and only the right half is shown. The emitter width of this structure is 75 nm. It is discretized with a grid of 74×20 nodes with a non-uniform spacing. The doping and Ge profiles along the symmetry line are given in Fig. 17. The base is 17.5 nm thick and the Ge content has the form of a box profile with a maximum Ge content of 18%. Basically, it is tried to follow the state-of-the-art doping and Ge profiles shown in [69].

The initial solution for the electrostatic potential is imported from the drift-diffusion or hydrodynamic model. When the correction of the electrostatic potential is smaller than a predefined value (e.g. 10^{-10} V in this simulation), convergence is achieved. Typical convergence behavior of the simulation is shown in Fig. 18. For $V_{BE} = 0.7$ V, $V_{CE} = 2.9$ V and a third-order expansion (the biggest system of equations with 12 437 920 unknown variables after elimination of the equations for odd l), the simulation time for the steady-state solution is over 12 hours on a single-core workstation. In this case, the maximum memory usage is about

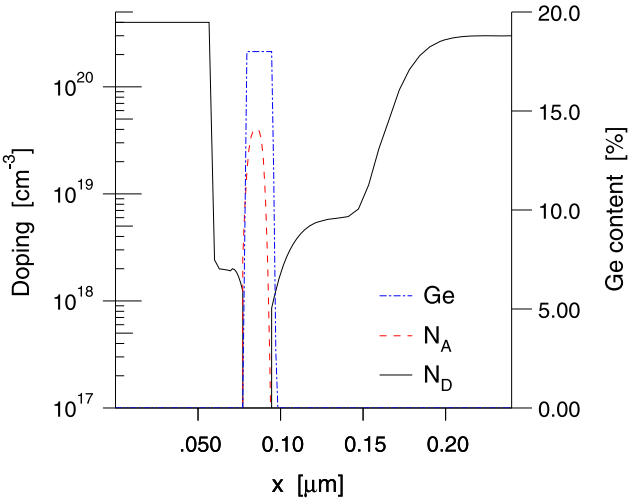

Fig. 17 1D doping and Ge profiles of the SiGe HBT for $y = 0$

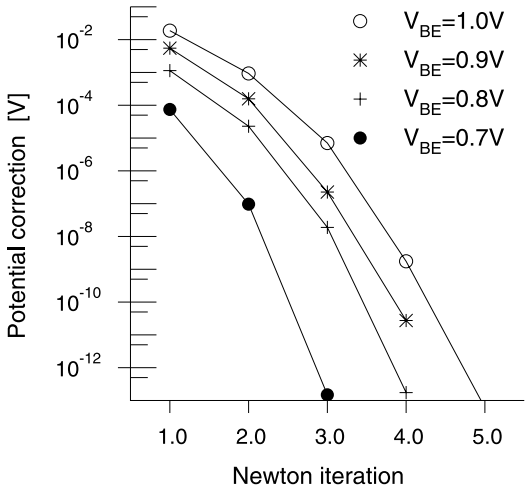

Fig. 18 Maximum value of the potential correction at each Newton-Raphson iteration for different V_{BE} values. $V_{CB} = 0.1$ V

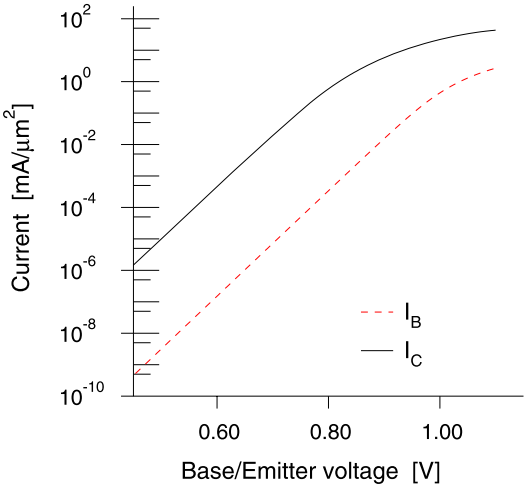

Fig. 19 Gummel plot. $V_{CB} = 0.1$ V

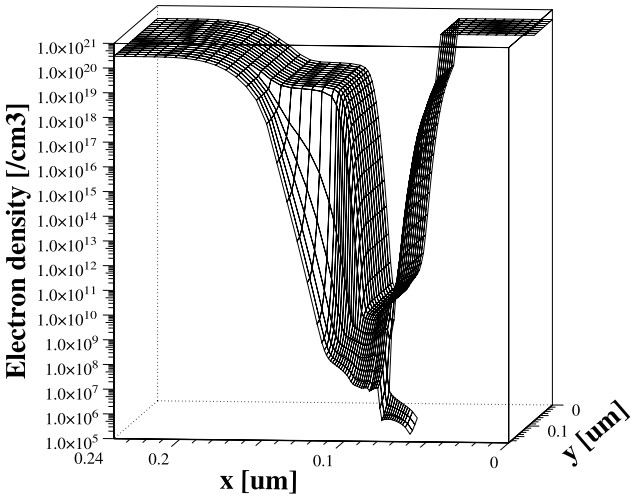

Fig. 20 Electron density in the two-dimensional simulation plane at $V_{BE} = 0.7$ V and $V_{CB} = 0.1$ V

26 GB. AC analysis requires about twice as much memory due to the complex numbers. Note that the simulation time and memory usage can change due to the internal parameters used in the iterative matrix solver, ILUPACK [70].

The Gummel plot is shown in Fig. 19. The current gain at $V_{BE} = 0.7$ V and $V_{CB} = 0.1$ V is about 2700. The Boltzmann equation solver is able to simulate the collector and base current without any problems over a range of several orders of magnitude, where the CPU time is much less sensitive to the bias condition than in the case of a Monte Carlo approach. Given the spatial grid and the maximum order of the spherical harmonics expansion, the main factor which determines the simulation time is the span of the total energy included in the simulation. For example, in the case of the SiGe HBT a larger energy span is required in the case of lower V_{BE} values or higher V_{CE} values.

The electron density in the two-dimensional simulation plane is shown in Fig. 20. Very small densities near the base-collector junction underneath the base contact can be simulated. The density is smooth and no artificial oscillations occur due to the successful stabilization of the Boltzmann equation. Since the six valleys in the conduction band are included in the simulation, detailed information for each valley is available. The valleys with the longitudinal mass aligned to x-, y-, and z-axis are denoted by x-, y-, and z-valley, respectively. In Fig. 21, the contribution of each valley to the electron density is shown. Since the x-valley has a higher minimum energy in the SiGe region due to the Ge content, its contribution to the electron density in that region is very small.

The cutoff frequency evaluated at constant $V_{CB} = 0.1$ V is shown in Fig. 22. The small-signal current gain at 10 GHz is used for extrapolation of the cutoff frequency.

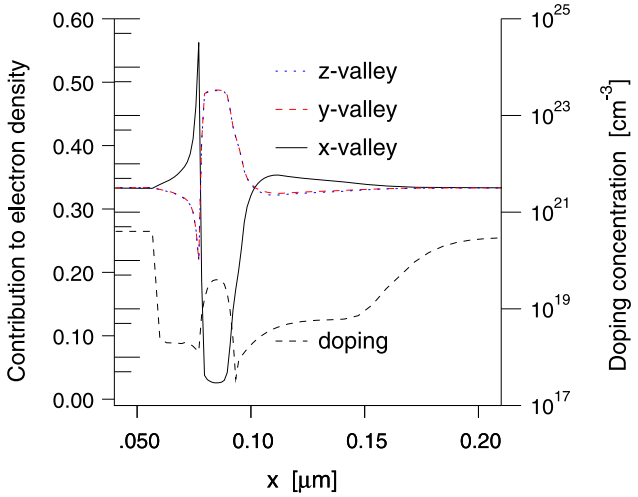

Fig. 21 Contribution of each valley to the electron density for $y = 0$ at $I_C = 5.79$ mA/µm^2 and $V_{CB} = 0.1$ V

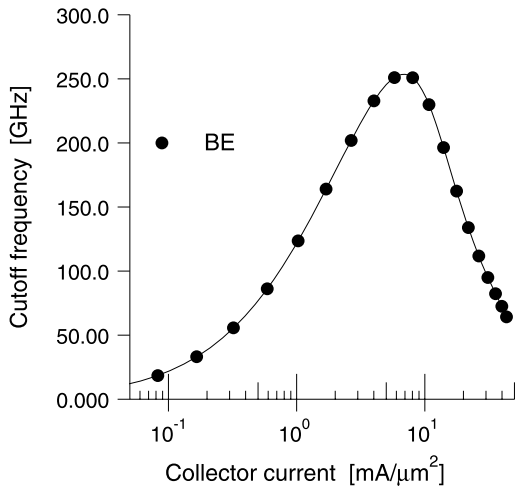

Fig. 22 Cutoff frequency. $V_{CB} = 0.1$ V

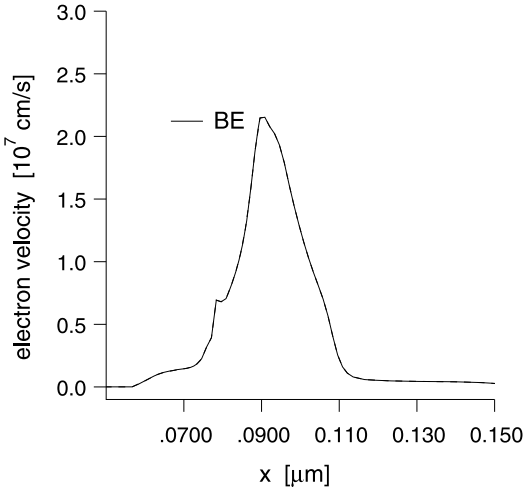

Fig. 23 Velocity profile for $y = 0$ at $I_C = 5.79$ mA/µm^2 and $V_{CB} = 0.1$ V

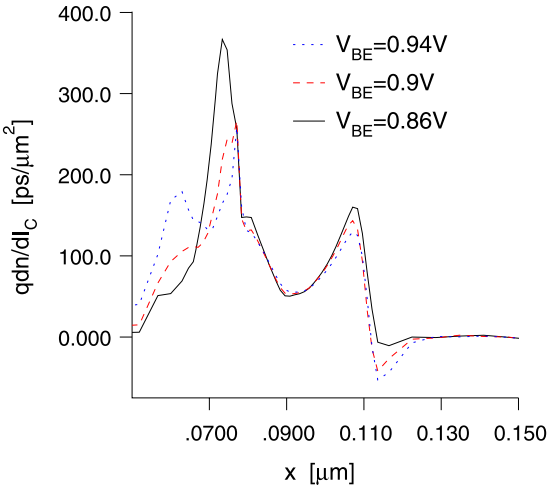

Fig. 24 Transit time distribution for $V_{BE} = 0.86$, 0.9, and 0.94 V. $V_{CB} = 0.1$ V

The peak cutoff frequency is 251 GHz in the range from $I_C = 6$ mA/µm^2 to $I_C = 8$ mA/µm^2. In order to predict the cutoff frequency and the corresponding collector current density correctly, accurate evaluation of the electron velocity is required. The electron velocity along the symmetry line is shown in Fig. 23. The maximum electron velocity is about two times the saturation velocity of silicon. In Fig. 24 the transit time distribution $(d\tau/dx)$ is shown for three different base/emitter voltages [71].

The output characteristics are shown in Fig. 25. The impact ionization model in [63] is exploited. The Early voltage obtained by the BE model is 9.5 V. In Fig. 26 the absolute value of the corresponding base currents is shown. The open base breakdown voltage evaluated from the collector/emitter bias at zero base current is 1.08 V.

The spectral intensity of the collector/collector current fluctuations is shown in Fig. 27. For low collector current densities it follows the shot noise expression $(2qI_C)$. The spatial origin of the terminal current fluctuations in the middle of the emitter window is shown in Fig. 28. The minimum noise figure is shown in Fig. 29. The electron noise current transit time, τ_n, which is given by [72, 73]

$$S_{I_B I_C}^{elec} = 2qI_C(e^{j\omega\tau_n} - 1), \tag{46}$$

is shown in Fig. 30.

4 Conclusion and future perspective

In this work we have reviewed a particular way to solve the Boltzmann equation, the spherical harmonic expansion approach. In this approach the Boltzmann equation is expanded with spherical harmonics, and the set of the resul-

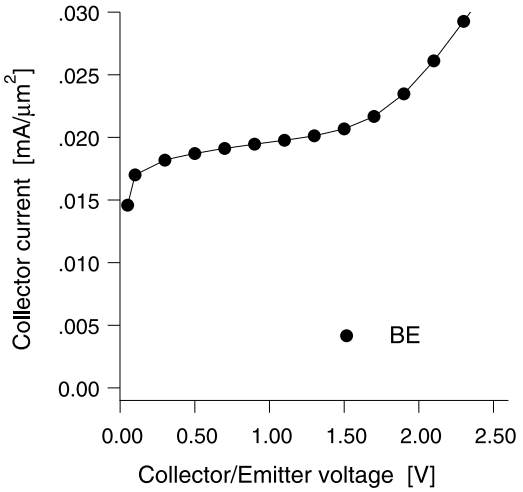

Fig. 25 Output characteristics. $V_{BE} = 0.7$ V

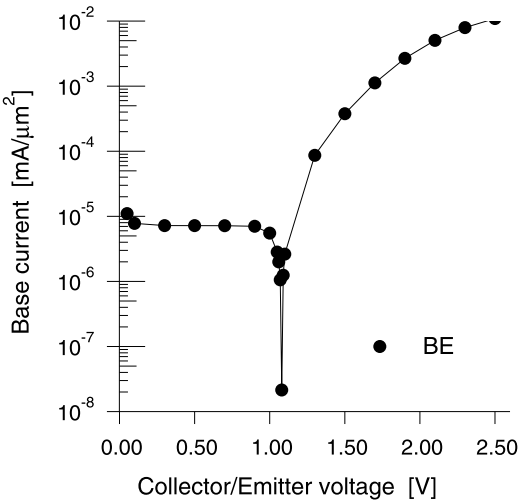

Fig. 26 Absolute value of the base current. $V_{BE} = 0.7$ V

tant balance equations is solved with standard numerical techniques. Since its properties are more similar to those of the classical TCAD tools, almost everything possible in the framework of the momentum-based device models can be (and has been) done with this approach but with a more physics-based model. Also, in this work, the recent progresses on this approach are shown. Especially, the fully-coupled scheme improves the robustness of the Newton scheme significantly.

Let us briefly mention some remaining topics. Although the inclusion of the Pauli principle is possible for bulk systems [74, 75], it has not yet been reported for devices. The complete inclusion of a full band structure is formulated in [5], but it has been applied only to holes by now. The expansion of the full band structure of electrons is difficult and might be approximated with the methods presented in [76].

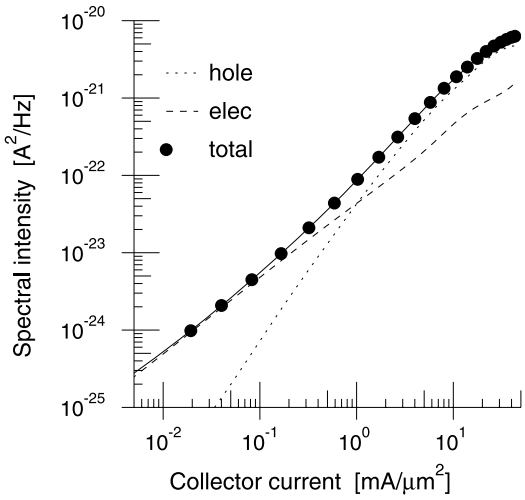

Fig. 27 Spectral intensity of the collector/collector current fluctuations at 10 GHz. $V_{CB} = 0.1$ V

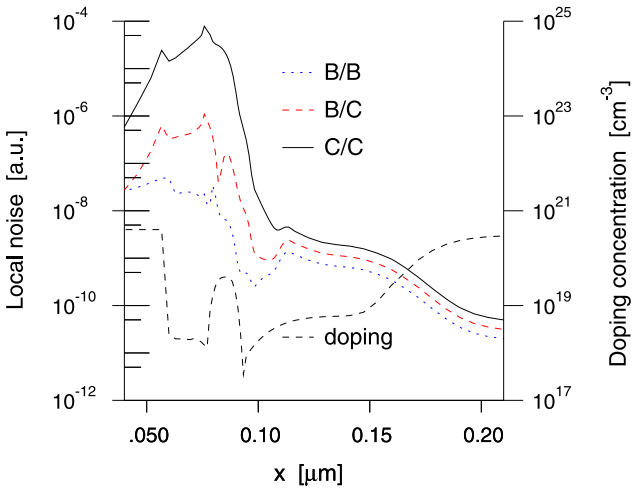

Fig. 28 Spatial origin of the terminal current fluctuations at 10 GHz. $V_{BE} = 0.82$ V and $V_{CB} = 0.1$ V. The absolute value is shown for the base/collector fluctuations

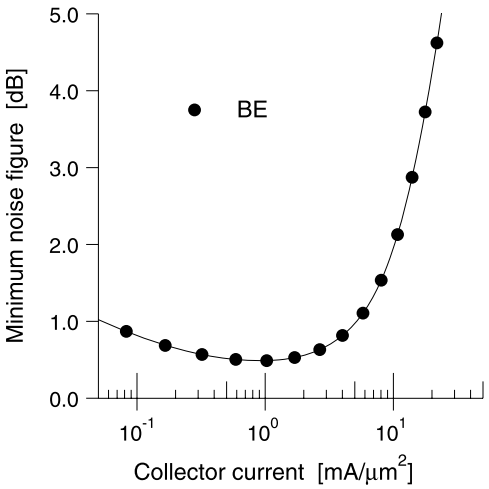

Fig. 29 Minimum noise figure at 10 GHz. $V_{CB} = 0.1$ V

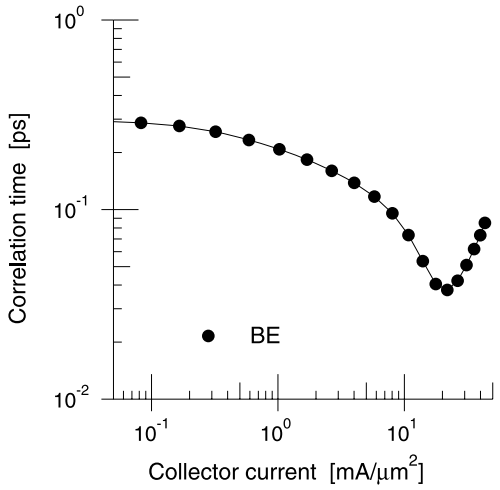

Fig. 30 Electron current noise transit time, τ_n at 10 GHz. $V_{CB} = 0.1$ V

Extension to large-signal operation is only shown by now for bulk simulations [77] and not for devices.

The advances in computers makes this computationally expensive method more and more attractive.

Acknowledgements The research leading to these results has received funding from the Deutsche Forschungsgemeinschaft under contract number JU 406/6-1. S.-M. Hong's work was partially supported by a Korea Research Foundation Grant by the Korean Government (MOEHRD) under contract number KRF-2007-357-D00159. The authors gratefully acknowledge Dr. M. Ramonas for providing the profiles of the SiGe HBT.

References

1. Thompson, S., et al.: 130 nm logic technology featuring 60 nm transistors, low-*k* dielectrics and Cu interconnects. Int. Technol. J. **06**(02), 5 (2002)
2. Nekovee, M., et al.: Failure of extended-moment-equation approaches to describe ballistic transport in submicrometer structures. Phys. Rev. B **45**(12), 6643 (1992)
3. Fischetti, M.V., et al.: Understanding hot-electron transport in silicon devices: is there a shortcut? J. Appl. Phys. **78**, 1058 (1995)
4. Shur, M.S.: Low ballistic mobility in submicron HEMTs. IEEE Electron Device Lett. **23**(9), 511 (2002)
5. Jungemann, C., et al.: Failure of moments-based transport models in nanoscale devices near equilibrium. IEEE Trans. Electron Devices **52**(11), 2404 (2005)
6. Madelung, O.: Introduction to Solid State Theory. Springer, Berlin (1978)
7. Jacoboni, C., Lugli, P.: The Monte Carlo Method for Semiconductor Device Simulation. Springer, Wien (1989)
8. van Kampen, N.G.: Stochastic Process in Physics and Chemistry. North-Holland, Amsterdam (1981)
9. Price, P.J.: Monte Carlo calculation of electron transport in solids. Semicond. Semimet. **14**, 249 (1979)
10. Kurosawa, T.: Monte Carlo calculation of hot electron problems. J. Phys. Soc. Jpn. **21**, 424 (1966)
11. Fawcett, W., et al.: Monte Carlo determination of electron transport properties in gallium arsenide. J. Phys. Chem. Solids **31**, 1963 (1970)
12. Reklaitis, A.: The calculation of electron transient response in semiconductors by the Monte Carlo technique. Phys. Lett. **13**, 367 (1982)
13. Reggiani, L.: Hot-Electron Transport in Semiconductors. Springer, Berlin (1985)
14. Nedjalkov, M., Vitanov, P.: Iteration approach for solving the Boltzmann equation with the Monte Carlo method. Solid-State Electron. **32**, 893 (1989)
15. Moglestue, C.: Monte Carlo Simulation of Semiconductor Devices. Chapman & Hall, London (1993)
16. Hess, K. (ed.): Monte Carlo Device Simulation: Full Band and Beyond. Kluwer, Boston (1991)
17. Fischetti, M.V., Laux, S.E.: Monte Carlo analysis of electron transport in small semiconductor devices including band-structure and space-charge effects. Phys. Rev. B **38**, 9721 (1988)
18. Jungemann, C., Meinerzhagen, B.: Analysis of the stochastic error of stationary Monte Carlo device simulations. IEEE Trans. Electron Devices **48**(5), 985 (2001)
19. Jungemann, C., et al.: Hierarchical 2–D DD and HD noise simulations of Si and SiGe devices, part II: results. IEEE Trans. Electron Devices **49**(7), 1258 (2002)
20. Banoo, K., Lundstrom, M.S.: Electron transport in a model Si transistor. Solid-State Electron. **44**, 1689 (2000)
21. Banoo, K., Lundstrom, M.: Direct solution of the Boltzmann transport equation in nanoscale Si devices. In: Proc. SISPAD, pp. 50–53 (2000)
22. Ringhofer, C.: Space-time discretization of series expansion methods for the Boltzmann transport equation. SIAM J. Numer. Anal. **38**, 442 (2000)
23. Ringhofer, C.: Numerical methods for the semiconductor Boltzmann equation based on spherical harmonics expansions and entropy discretizations. Transp. Theory Stat. Phys. **31**(4–6), 431 (2002)
24. Ringhofer, C.: A mixed spectral-difference method for the steady state Boltzmann-Poisson system. SIAM J. Numer. Anal. **41**(1), 64 (2003)
25. Ringhofer, C., et al.: Moment methods for the semiconductor Boltzmann equation in bounded position domains. SIAM J. Numer. Anal. **39**, 1078 (2001)
26. Baraff, G.A.: Maximum anisotropy approximation for calculating electron distributions; application to high field transport in semiconductors. Phys. Rev. **133**(1A), A26 (1964)
27. Ventura, D., et al.: Multidimensional spherical harmonics expansion of Boltzmann equation for transport in semiconductors. Appl. Math. Lett. **5**, 85 (1992)
28. Vecchi, M.C., Rudan, M.: Modeling electron and hole transport with full-band structure effects by means of the spherical-harmonics expansion of the BTE. IEEE Trans. Electron Devices **45**(1), 230 (1998)
29. Jungemann, C., et al.: Stable discretization of the Boltzmann equation based on spherical harmonics, box integration, and a maximum entropy dissipation principle. J. Appl. Phys. **100**, 024502 (2006)
30. Smirnov, S., Jungemann, C.: A full band deterministic model for semiclassical carrier transport in semiconductors. J. Appl. Phys. **99**, 063707 (2006)
31. Hong, S.-M., Jungemann, C.: Simulation of magnetotransport in nanoscale devices. In: International Conference on Solid State and Integrated Circuits Technology, pp. 377–380 (2008)
32. Liang, W., et al.: 2-D MOSFET modeling including surface effects and impact ionization by self-consistent solution of the Boltzmann, Poisson, and hole-continuity equations. IEEE Trans. Electron Devices **44**(2), 257 (1997)
33. Gnudi, A., et al.: Two-dimensional MOSFET simulation by means of a multidimensional spherical harmonics expansion of the Boltzmann transport equation. Solid-State Electron. **36**(4), 575 (1993)

34. Hong, S.-M., et al.: A deterministic Boltzmann equation solver for two-dimensional semiconductor devices. In: Proc. SISPAD, pp. 293–296 (2008)
35. Goldsman, N., et al.: Advances in the spherical Harmonic-Boltzmann-Wigner approach to device simulation. Superlattices Microstruct. **27**, 159 (2000)
36. Hennacy, K.A., Goldsman, N.: A Generalized Legendre polynomial/sparse matrix approach for determining the distribution function in non-polar semiconductors. Solid-State Electron. **36**, 869 (1993)
37. Hennacy, K.A., et al.: Deterministic MOSFET simulation using a generalized spherical harmonic expansion of the Boltzmann equation. Solid-State Electron. **38**, 1485 (1995)
38. Rahmat, K., et al.: Simulation of semiconductor devices using a Galerkin/spherical harmonic expansion approach to solving the coupled Poisson-Boltzmann system. IEEE Trans. Comput.-Aided Des. **15**(10), 1181 (1996)
39. Lin, C.-K., et al.: Frequency domain analysis of the distribution function by small signal solution of the Boltzmann and Poisson equations. In: Proc. SISPAD, pp. 39–42 (1999)
40. Jungemann, C.: A deterministic approach to RF noise in silicon devices based on the Langevin Boltzmann equation. IEEE Trans. Electron Devices **54**(5), 1185 (2007)
41. Jungemann, C., et al.: New highly efficient method for the analysis of correlation functions based on a spherical harmonics expansion of the BTE's Green's function. In: Proc. IWCE, pp. 45–48 (1994)
42. Korman, C.E., Mayergoyz, I.D.: Semiconductor noise in the framework of semiclassical transport. Phys. Rev. B **54**, 17620 (1996)
43. Jungemann, C., Meinerzhagen, B.: A Legendre polynomial solver for the Langevin Boltzmann equation. J. Comput. Electron. **3**, 157 (2004)
44. Hong, S.-M., Jungemann, C.: Deterministic simulation of SiGe HBTs based on the Boltzmann equation. In: Proc. ESSDERC, pp. 170–173 (2008)
45. Hong, S.-M., Jungemann, C.: Investigation of noise performance of SiGe HBTs by deterministic simulation of Boltzmann equation in two-dimensional real space. In: International Conference on Noise in Physical Systems and 1/f Fluctuations, pp. 573–576 (2009)
46. Brunetti, R., et al.: Diffusion coefficient of electrons in silicon. J. Appl. Phys. **52**, 6713 (1981)
47. Herring, C., Vogt, E.: Transport and deformation-potential theory for many-valley semiconductors with anisotropic scattering. Phys. Rev. **101**(3), 944 (1956)
48. Goldsman, N., et al.: A physics-based analytical/numerical solution to the Boltzmann transport equation for use in device simulation. Solid-State Electron. **34**, 389 (1991)
49. Marshak, A.H., van Vliet, K.M.: Electrical current in solids with position-dependent band structure. Solid-State Electron. **21**, 417 (1978)
50. Abramowitz, M., Stegun, I.A.: Handbook of Mathematical Functions. Dover, New York (1972)
51. Jin, S., et al.: Theoretical study of carrier transport in silicon nanowire transistors based on the multisubband Boltzmann transport equation. IEEE Trans. Electron Devices **55**, 2886 (2008)
52. Berman, A., Plemmons, R.J.: Nonnegative Matrices in the Mathematical Sciences. Computer Science and Applied Mathematics. Academic Press, New York (1979)
53. Varga, R.S.: Matrix Iterative Analysis. Series in Automatic Computation. Prentice-Hall/Englewood Cliffs, New Jersey (1962)
54. Jungemann, C., Meinerzhagen, B.: Hierarchical Device Simulation: The Monte-Carlo Perspective. Computational Microelectronics. Springer, Wien (2003)
55. Branin, F.H.: Network sensitivity and noise analysis simplified. IEEE Trans. Circuit Theory **20**, 285 (1973)
56. Bonani, F., et al.: An efficient approach to noise analysis through multidimentional physics-based models. IEEE Trans. Electron Devices **45**(1), 261 (1998)
57. Hong, S.-M., et al.: Governing equations of the terminal current Green's functions and their application to derivation of the Nyquist theorem for multi-terminal semiconductor devices. J. Appl. Phys. **102**, 073717 (2007)
58. Jungemann, C.: Transport and noise calculations for nanoscale Si devices based on the Langevin Boltzmann equation expanded with spherical harmonics. J. Comput. Theory Nanosci. **5**(6), 1152 (2008)
59. Gritsch, M., et al.: Influence of generation/recombination effects in simulations of partially depleted SOI MOSFETs. Solid-State Electron. **45**, 621 (2001)
60. Gritsch, M., et al.: Revision of the standard hydrodynamic transport model for SOI simulation. IEEE Trans. Electron Devices **49**(10), 1814 (2002)
61. Polsky, B., et al.: On negative differential resistance in hydrodynamic simulation of partially depleted SOI transistors. IEEE Trans. Electron Devices **52**, 500 (2005)
62. Lombardi, C., et al.: A physical based mobility model for numerical simulation of nonplanar devices. IEEE Trans. Comput.-Aided Des. **7**, 1164 (1988)
63. Thoma, R., et al.: An improved impact–ionization model for high–energy electron transport in Si with Monte Carlo simulation. J. Appl. Phys. **69**, 2300 (1991)
64. Jungemann, C., et al.: Impact of the floating body effect on noise in SOI devices investigated by hydrodynamic simulation. In: Proc. SISPAD, pp. 235–238 (2004)
65. Thoma, R., et al.: Hydrodynamic equations for semiconductors with nonparabolic bandstructures. IEEE Trans. Electron Devices **38**(6), 1343 (1991)
66. Mains, R.K., et al.: Simulation of GaAs IMPATT diodes including energy and velocity transport equations. IEEE Trans. Electron Devices **30**(10), 1327 (1983)
67. Jin, W., et al.: Shot-noise-induced excess low-frequency noise in floating-body partially depleted SOI MOSFET's. IEEE Trans. Electron Devices **46**(7), 1180 (1999)
68. Klaassen, D.B.M., et al.: Unified apparent bandgap narrowing in n- and p-type silicon. Solid-State Electron. **35**, 125 (1992)
69. Fox, A., et al.: SiGe HBT module with 2.5 ps gate delay. In: IEEE Tech. Dig. IEDM, pp. 731–734 (2008)
70. Bollhöfer, M., Saad, Y.: ILUPACK—preconditioning software package. Release 2.2 available online at www-public.tu-bs.de/~bolle/ilupack/ (2008)
71. van den Biesen, J.: A simple regional analysis of transient times in bipolar transistors. Solid-State Electron. **29**, 529 (1986)
72. Rudolph, M., et al.: An HBT noise model valid up to transit frequency. IEEE Electron Device Lett. **20**(1), 24 (1999)
73. Niu, G., et al.: RF linearity characteristics of SiGe HBTs. IEEE Trans. Microwave Theory Tech. **49**(9), 1558 (2001)
74. Piazza, A.J., et al.: A physics-based semiconductor noise model suitable for efficient numerical implementation. IEEE Trans. Comput.-Aided Des. **18**(12), 1730 (1999)
75. Jungemann, C.: A deterministic solver for the Langevin Boltzmann equation including the Pauli principle. In: SPIE: Fluctuations and Noise (2007) 660007-1–660007-12
76. Pham, A.T., et al.: A full-band spherical harmonics expansion of the valence bands up to high energies. In: Proc. SISPAD, pp. 361–364 (2006)
77. Jungemann, C., Meinerzhagen, B.: A frequency domain spherical harmonics solver for the Langevin Boltzmann equation. In: International Conference on Noise in Physical Systems and 1/f Fluctuations. AIP Conf. Proc., pp. 777–782 (2005)